UNIVERSITA' DEGLI STUDI DI TORINO
FACOLTÁ DI SCIENZE MATEMATICHE, FISICHE E NATURALI
CORSO DI LAUREA IN FISICA DELLE INTERAZIONI
FONDAMENTALI

INDIRIZZO SPERIMENTALE

Search for η transitions between bottomonia in the Belle experiment at KEK

Relatore

Prof. Ezio Menichetti

Candidato

Umberto Tamponi

Correlatore

Dott. Roberto Mussa

Sessione Luglio 2011
Anno Accademico 2010/1011

Contents

Chapter 1

Introduction

1.1 The Heavy quarkonium

The heavy quarkonium is a bound state of a heavy quark and its anti-quark; if the two quarks are c and $\bar{c}$ the state is commonly referred as "charmonium", while "bottomonium" is the common name for mesons containing a $b\bar{b}$ pair. The Schroedinger equation for this system can be separate into a spatial and a radial part, like it's commonly done when dealing with other bound system of a particle with its own anti-particle such as positronium, thus naturally leading to a spectroscopic-like arrangement of the quarkonium states (Figg. 1.1 and 1.2). In this framework each

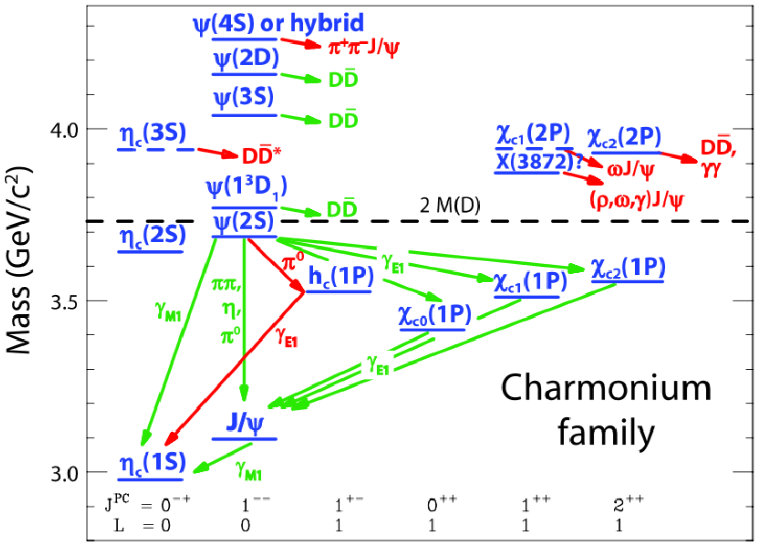

Figure 1.1: Charmonium spectrum, adapted from [6].

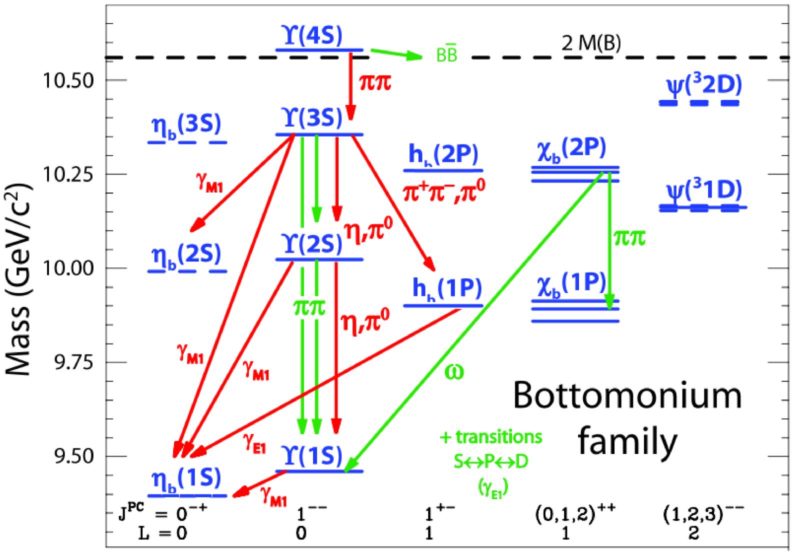

Figure 1.2: Bottomonium spectrum, adapted from [6].

state is labeled with its momentum eigenvalue J, its radial excitation number n and the number of possible spin configurations $2S + 1$. Since the quarks have spin $s = 1/2$, like in the positronium case both spin singlets ($s_{tot} = 0$) and spin triplets ($s_{tot} = 1$) are possible, while no isospin degeneration is observed since every bottomonium state must have $I = 0$. Despite these similarities between bottomonium and positronium, a major difference arises from the nature of the binding potential. While the positronium is essentially an electromagnetic state, describable in terms of classical potential or, looking for a more suitable framework, using the QED perturbative approach, the dominant interaction in $b\bar{b}$ states is the strong one. This means that, together with radiative transitions, also hadronic transition are allowed between quarkonium states, when allowed by
A set of selection rules based on the conservation of total momentum, C-parity and P-parity determine which kind of transitions, both radiative and hadronic ones, are allowed and which are forbidden:

- Radiative transitions $(b\bar{b})' \to \gamma(b\bar{b})$ are possible only between states that differs by a unit of angular momentum ($|\Delta l| = 1$), so the possible transitions are $P \leftrightarrow S$ and $D \leftrightarrow P$ and $^3S \leftrightarrow^1 S$. The same kind of transition can obviously happen with the emission of a vector meson like the ω.

- Hadronic transitions with a single scalar meson (π^0, η, η') can connect, if we consider only the angular momentum conservation, each pair of states. On the other hand the conservation of C- and P-parity forbids processes like $1^{--} \leftrightarrow (0,1,2)^{-+}$, namely $\Upsilon(nS) \to \pi^0, \eta\chi_{bJ}(mP)$, while transitions like $\Upsilon(nS) \to (\pi^0, \eta)(\Upsilon(mS), h_b(mP))$ are still possible. Since all these transition are mediated by the strong interaction, we must take into account also the (partial) conservation of the Isospin that greatly suppress the π^0 transition with respect to the η, η' ones. Finally, if we consider the phase space available for each transition, we found that the only single-scalar transitions that remains available and unsuppressed are $\Upsilon(nS) \to \eta\Upsilon(mS)$.

- Hadronic transitions with two scalar mesons ($\pi^+\pi^-$, $\pi^0\pi^0$) are the dominant transitions between $\Upsilon(nS)$ states below the open beauty threshold. The conservation of the isospin requires $\mathcal{B}(Y(nS) \to \pi^+\pi^-\Upsilon(mS)) \approx 2 \times \mathcal{B}(Y(nS) \to \pi^0\pi^0\Upsilon(mS))$.

1.2 Theoretical models in heavy quarkonium physics

Many theories has been developed to describe the experimental results on both transitions and annihilation products of the quarkonia. A simple potential model allows to check the relativistic or non relativistic nature of the charmonium and make some prediction on the masses of the states. The Non-Relativistic Quantum-Chormodimanics (NRQCD), which is based on a series expansion of the QCD Hamiltonian, can lead to more precise results and can also provide predictions on the branching fractions for both transitions and annihilations. The Lattice calculation, which is a numerical technique used in order to perform calculation within the path integral theory framework, is used to make numerical prediction on soft and ultra-soft processes. For different reasons, all these theories involves approximations: the static potential theory is fully solvable but is based on a phenomenological potential, the NRQCD is a perturbative approach and the lattice, even if the calculations are performed within an exact theory, stills remains limited by the available computational resources.

1.2.1 The potential model and the limits of the non relativistic approach

The simplest way to describe a bound state is, in general, to solve a non-relativistic Schroedinger equation with a suitable potential.

The bottomonium spectrum pattern suggests the presence of a radial binding potential with a Coulombian-like behavior; the comparison between the charmonium, positronium and harmonic oscillator spectrum (Figure 1.3) shown that actually the strong potential acts as an hybrid between a Coulumbian potential and an harmonic one. Since it is known that the strong interaction becomes attractive at long distances, as no free quark has been observed, a potential model used for the description of the strong interactions must contains at least two different terms: a Coulombian-like term that dominates at short distances, as suggested by the comparison between charmonium ad positronium spectrum, and a confinement term that, at long distances, accounts for the quark confinement summarizing the asymptotic freedom effects.

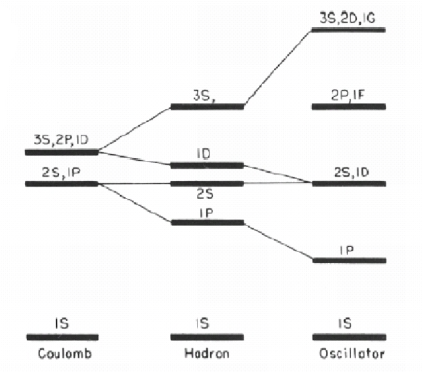

Figure 1.3: The charmonium energy levels compared with the predictions obtained with a Coulombian-like or harmonic potential.

One of the most used model is the Cornell potential (Fig. 1.4), defined as:

$$V(r) = -\frac{4\alpha_s}{3r} + \sigma r,$$

where α_s is the strong coupling constant and σr is the confinement term.

The potential parameters are usually tuned on the experimental data of one resonance, and then they are used to calculate the expected masses of all the other states.

A study done by Quigg and Rosner with a modified Cornell-like potential $V(r) = C \cdot ln(r/r_0)$ that phenomenologically interpolates the $1/r$ trend at short distances and the r dependence at long distance, leads to an estimation of the mean quadratic velocity of the heavy quark, obtaining $< v^2(c) > \approx 0.24$ for the c quark in the J/ψ and $< v^2(b) > \approx 0.08$ for the b quark in the $\Upsilon(1S)$; thus a non relativistic approach is a crude approximation in charmonia description, but it is substantially correct in describing the bottomonium states. Whitin the potential model frame it is possible to describe the fine and hyperfine splitting, which are sensitive to the Lorentz structure of the interaction, by introducing a spin-spin interaction term in the form:

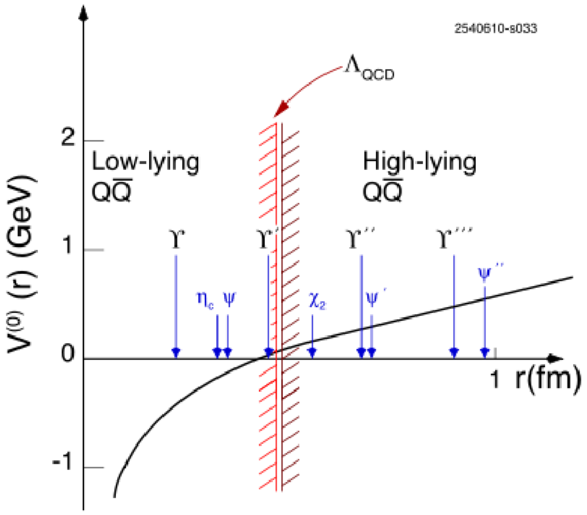

Figure 1.4: A Cornell-like potential tuned for bottomonium states. The potential parameters are extracted from the $\Upsilon(1S)$ and $\Upsilon(2S)$ experimental data.

$$V_{SS}(r) = \frac{\sigma_Q \cdot \sigma_{\bar{Q}}}{6m_Q^2} \nabla^2 V(r)$$

A complete derivation of the mass formula can be found in [7].

The spectra obtained with this technique are shown in figure 1.5 and 1.6, together with the current experimental measurements of bottomonium and charmonium levels.

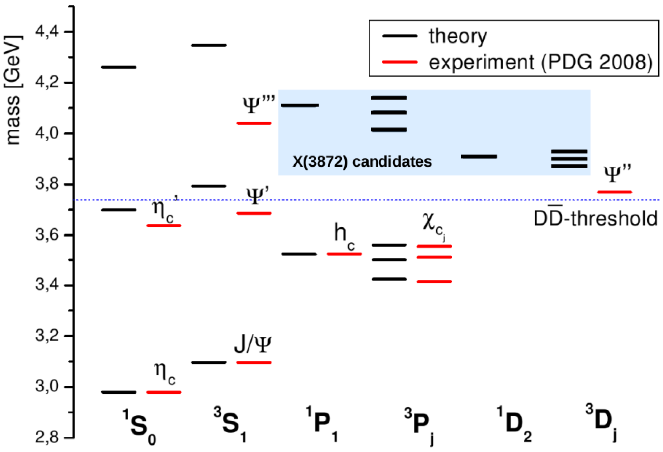

Figure 1.5: Prediction on Charmonium spectrum with a Cornell potential model, $\alpha_s = 0.290,\ m_b = 1.2185 GeV,\ \sigma = 1.306 GeV/fm$

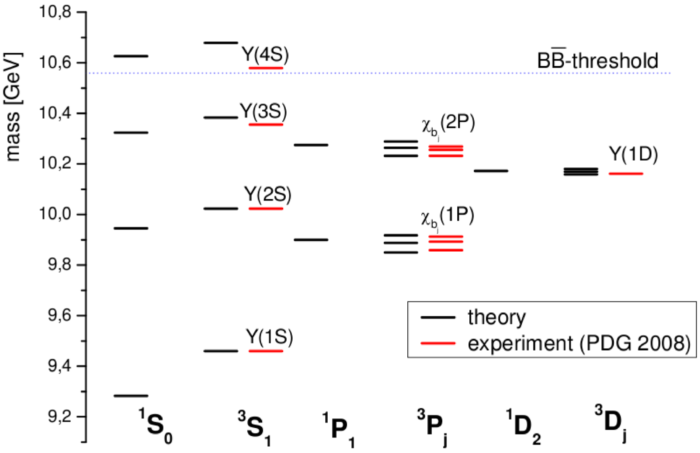

Figure 1.6: Prediction on Bottomonium spectrum with a Cornell potential model, $\alpha_s = 0.388,\ m_b = 4.7645 GeV,\ \sigma = 1.02 GeV/fm$

1.2.2 Non-relativistic QCD

The Non-Relativistic QCD (NRQCD) is one of the most common framework used in making prediction on partial width of the transitions among bottomonium states. The foundation of NRQCD is the statement that, since the typical quark velocity $v(q)$ is small when compare with the QCD scale, the Lagrangian containing the chosen potential model can be expanded in series of $v(q)$.
The study of bottomonium shows a broad scale of energies involved in the interaction, usually divided into a three level hierarchy:

- Hard scale, for process with energy $\approx m_q$, for which a perturbative approach is allowed.
- Mid scale, with typical energy of $\approx m_q v$.
- Soft scale, characterized by energies $\approx m_q v^2$, for which a perturbative approach is no more possible.

Processes with very different energy scales can contribute to the same physical process, as shown in 1.7.

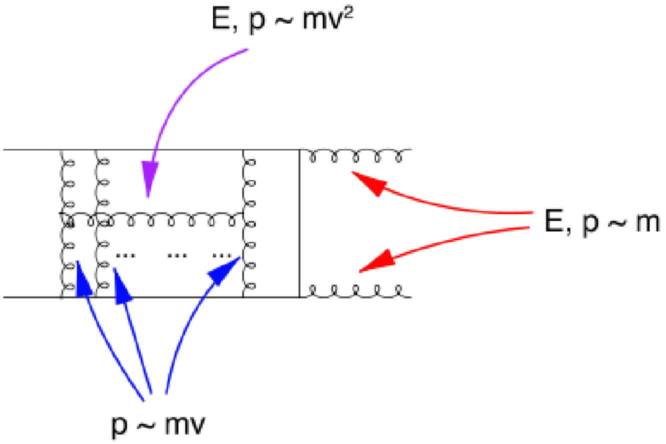

Figure 1.7: A Feynman diagram showing interaction at different energy scales

One of the possible declinations of the NRQCD approach is the QCD Multipole Expansion formalism (QCDME): when dealing with hadronic transitions the QCD interaction Hamiltonian can be expanded in a series of multipoles, reminding the usual electromagnetic multipole series expansion:

$$H_I = \int d^3x Q(x) t^n [x \cdot E_a(x) + \sigma \cdot B_a(x)] Q(x) + ...$$

where t^a are the SU(3) generators and the E and B fields are the chromoelectric and chromomagnetic fields.
The presence of the SU(3) generators make a single H_I interaction able to change the color state of a $Q\bar{Q}$ state from singlet to octuplet: this means that every physical transition must include at least two single interactions: the first one turns the singlet state into octuplet, and the second one re-turns the octuplet state into an observable state. This behavior, which is not present in the electromagnetic interaction, can be interpreted as the emission of at least two gluons in each hadronic transition, while electromagnetic transitions can proceed via a single photon emission, as it indeed happens in decays such as $\Upsilon(2S) \to \chi_{bJ}\gamma$.

In the QCDME formalism the $\Upsilon(2S) \to \Upsilon(1S)\eta$ is described by with one chromoelectric transition E1, which does not changes the spin of the b quarks, followed by a M1 chromomagnetic transition, which is responsible for the spin flip of the heavy quark. Those kind of transition are predicted suppressed by the presence, in the pure chromomagnetic term, of an additional power of v.

1.2.3 Lattice QCD

The Lattice QCD is numerical approach to the strong interaction problem based on the path integral formalism.

The basic assumption of this approach is that the transition amplitude between two states can be expressed as the sum of single amplitudes calculated on every possible path in the phase space that connects the initial and the final states, each one weighted by the value of its classical action. This theory can be used, under the additional assumptions that the more probable path is the classical one and that the whole amplitude can be expressed as a perturbative series in the phase space around the classical path, to perform analytical calculation, obtaining the same results that can be obtained by the perturbative approach.

The general aspect of a path integral can be shown also in the simplest case: a single particle propagator in one dimension, from the position x_0 at the time t_0 to the point x_1 at time t_1 can be expressed by:

$$< x_1, t_1 | x_0, t_0 >= \lim_{n\to\infty} k^{n/2} \int Dx \; exp[\int Ldt]$$

Where $\int Dx$ represents the sum over all the possible path connecting (x_0, t_0) and (x_1, t_1), $k = \frac{m}{2\pi i\hbar\Delta t}$ is the normalization constant and $\int Ldt$ is the classical action associated to each path.

Even if the integration is usually performed by introducing a series expansion that makes possible the factorization of the interaction terms leaving a sum of free particle propagators, this is in principle an exact theory. Therefore is possible to perform numerical calculation and obtain matrix element also for soft or ultra-soft scale processes in QCD, that are inaccessible with a perturbative approach.

From the numerical point of view, the key of this technique is the evaluation of the quantum operators on a discretized phase space; the transition amplitude is calculated by the path integration along concatenated loops.

The computational resource required to perform those calculation are the major limiting factor to the use of this technique. In the bottomonium study, in particular, the wide range of energies involved in the interaction requires loops too extended in the phase space to be calculated with the actual computational resources.

Nevertheless a lattice approach can be useful associated with a NRQCD calculation:

the expectation values of the operators extracted from the power expansion in series of $< v >$ can be calculated on the lattice phase space to obtain prediction on experimental observables such as masses, width and branching ratios.

The Lattice QCD has been used also to check the consistency of the Cornell's potential: in figure 1.8 the comparison between the static potential and the Lattice prediction is shown.

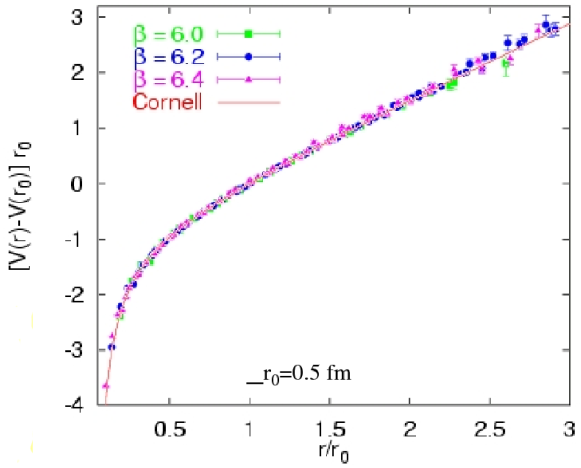

Figure 1.8: The Cornell potential compared with the Lattice QCD predictions

1.3 The $\Upsilon(2S) \to \Upsilon(1S)\eta$ transition

The subject of this thesis is the $\Upsilon(2S) \to \Upsilon(1S)\eta$ hadronic transition.
This transition has been, since the early studies on heavy quarkonia, one of the most evident differences between charmonium and bottomonium. In charmonium, the $\eta \to \gamma\gamma$ band is as visible as the double cascade transitions though $\chi_{c1,2}$ states, with a branching ratio $\mathcal{B} = 3.13 \pm 0.08\%$. On the other side, in bottomonium, a weak evidence of the transition has only recently been reported by CLEO [8].

The NRQCD predicts that this transition should be sensitive to the quark mass m_q, scaling with $(p^*)^3/m_q^4$ [9], where p^* is the η momentum in the $\Upsilon(2S)$ frame. Therefore the ratio between partial widths $\Gamma(\Upsilon(2S) \to \eta\Upsilon(1S))/\Gamma(\psi' \to \eta J/\psi)$ is expected to be approximatively 0.25%, and therefore a branching ratio $\mathcal{B} \approx 8 \times 10^{-4}$ is predicted by the CLEO collaboration [8].
Recent theoretical studies predict a branching fraction between 3×10^{-4} and 4×10^{-4} [10][11].
The experimental measurement by CLEO is a factor 4 weaker than the prediction from the CLEO collaboration, and a factor 2 weaker than the prediction from [10] and [11]. The isospin-violating transition $\Upsilon(3S) \to \pi^0\Upsilon(1S)$, predicted with a $\mathcal{B} \approx 6.5 \times 10^{-4}$, has not been observed. Figure 1.9 shows the CLEO results on the η transitions.

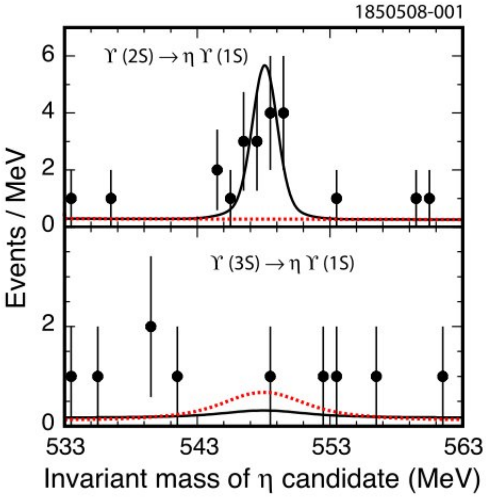

Figure 1.9: CLEO results on $\Upsilon(nS) \to \Upsilon(1S)\eta$ transitions

The discrepancy between theory and experiment is even more striking at $\Upsilon(4S)$

energy, as Babar [12] observed the totally unexpected $\eta\Upsilon(1S)$ transition, with a branching ratio $\mathcal{B}(\eta\Upsilon(1S)) = 2.5\ \times\mathcal{B}(\pi\pi\Upsilon(1S)))$.

All $\Upsilon(nS) \to \eta\Upsilon(mS)$ must have the same angular distribution, as this decay is described by only one independent helicity amplitude. The quantum numbers J^{PC} of this transitions are $1^{--} \to 0^{-+}1^{--}$, so it must proceed with a pure P-wave amplitude in order to preserve both the P- and C-parity. The angular distribution of the eta direction in CM frame is thus proportional to $(1{+}\cos^2\theta)$.

The subject of this thesis is the measurement of the branching fraction of the $\Upsilon(2S) \to \eta\Upsilon(1S)$ transition using the sample of 158 Millions of $\Upsilon(2S)$ collected by the Belle experiment. The analysis is performed reconstructing the final states $\Upsilon(1S) \to e^+e^-$, $\Upsilon(1S) \to \mu^+\mu^-$, $\eta \to \gamma\gamma$ and $\eta \to \pi^+\pi^-\pi^0$. In order to minimize the possible biases a blind optimization of the selection criteria based on a full Montecarlo simulation of both signal and background channels is performed.

Chapter 2

The Belle Experiment

2.1 The B-factories

Among all the bottomonium states that, having quantum numbers 1^{--}, can be directly produced in e^+e^- collisions, the $\Upsilon(4S)$ is the first with invariant mass above the threshold for the production of $B\bar{B}$ pairs. The $B\bar{B}$ pair is produced in a coherent state, and this characteristic makes an e^+e^- collider with $\sqrt{s} = 10.58$ GeV/c^2 the perfect environment to study the phenomenology of the B mesons and, therefore, to measure the CP-violation parameters related to the b quark. An asymmetric e^+e^- collider with high luminosity, tuned at $\sqrt{s} = M(\Upsilon(4S))$ energy, is commonly called B-factory.

One of the main goals of these facilities is the study of the oscillation in B meson system, the analogue of the phenomenon observed in the $'70$ in the K system. The strategy is to calculate the mean life of B and $\bar{B}$, produced together in a coherent state, measuring the distance between their production and decay points, following what was already done by Cronin and Fitch for the K system. In the B meson case the decay time is much shorter ($\tau = 1.5 \cdot 10^{-12}$) than in the K case, and they are produced almost at rest, so the distance from the primary vertex (i.e the decay point of the $\Upsilon(4S)$, that coincides with the collision point of the e^+e^- pair) and the decay point can not be easily measured ($c\tau \approx 460\mu m$ for a B^0).

The solution to this problem is to produce the $B\bar{B}$ system in a boosted frame: the boost magnifies the paths in the laboratory frame, making them measurable with a sufficient precision. This is the reason why a typical feature of the B-factories is large energy asymmetry between the two colliding beams, with a consequent boost between the frame of the e^+e^- pair and the laboratory frame. Both BaBar and Belle had $E_{e^-} \approx 2E_{e^+}$.

Even if B-factories have been designed and optimized for the CP-violation measurements, they revealed a high potential also in other branches of particle physics, in particular the quarkonium spectroscopy, with the possibility of produce directly all the Υ resonances and, via initial state radiation, the 1^{--} resonances of charmonium. The Initial State Radiation (ISR) is a second order electromagnetic process consisting in the emission of a real photon by one of the two colliding particles; the resulting collision will happen with a reduced energy in the center of mass $\sqrt{s'}$. By reconstructing the emitted ISR photon is possible to determine $\sqrt{s'}$ as $\sqrt{s'} = \sqrt{s} - E_{\gamma\ ISR}$.

Other topics that can be studied in a B-factory include the two photon physics, due to the high $\gamma\gamma$ cross section related to the high luminosity of the collider, the τ physics, the test of conservation law such the lepton number conservation in the $\Upsilon \rightarrow l^+l^-$ process and, recently, also the search for dark matter in $\Upsilon(nS)$ decays.

2.2 The KEKB accumulation ring

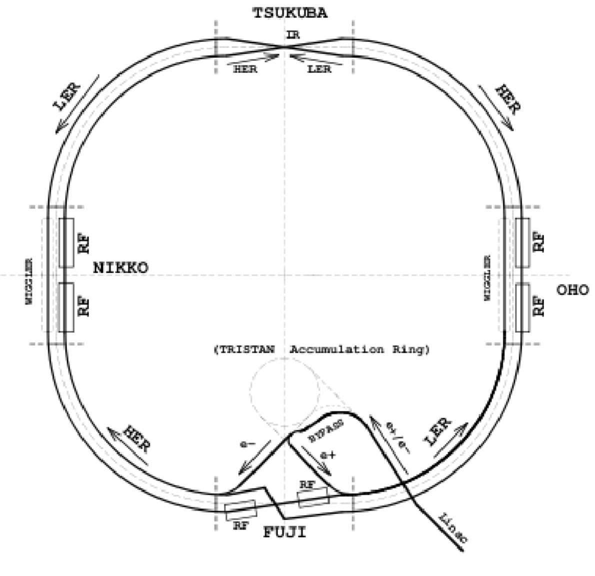

Figure 2.1: The KEKB accelerator complex

The KEKB [13] is an high-luminosity electron-positron collider located at the KEK (High Energy Accelerator Research Organization) in Tsukuba, Japan. The accelerator complex consists in a 600 m long linear accelerator (LINAC) connected with two storage rings (Fig. 2.1). Electron and positron bounces are accelerated by the LINAC and then injected into the two separated rings; since the bounces acceleration is performed only by the LINAC, the injection can proceed continuously minimizing the detector dead time. During the Belle data taking the two beams were kept at different energies, providing non symmetric collisions; the electrons were injected in the High Energy Ring (HER) at the energy of $E_{HER} \approx 8$ GeV, while the positrons were injected in the Low Energy Ring (LER) with an energy of $E_{LER} \approx 3.5$ GeV. Table 2.1 summarizes the energies of the HER and LER beams used during the Belle experiment to provide different $\sqrt{s}$. Both the HER and LER energies were changed when changing $\sqrt{s}$ in order to keep the center-of-mass boost at the constant value of $\beta_{CM} = 0.39$.

Table 2.1: HER and LER energies

$\sqrt{s}$ $[GeV]$	Resonance	HER energy [GeV]	LER energy [GeV]
9.4603	$\Upsilon(1S)$	7.151100	3.128600
1.0023	$\Upsilon(2S)$	7.575000	3.314100
1.0355	$\Upsilon(3S)$	7.826200	3.424000
1.0579	$\Upsilon(4S)$	7.998800	3.499500
1.0860	$\Upsilon(5S)$	8.215000	3.594100

After the injection three groups of radio-frequency cavities (two placed along the HER, one along the LER) were used to sustain the energy of the beams.
In order to avoid parasitic collisions and keep the beam background as low as possible the two beams had a crossing angle of 22 $mrad$ in the zy plane. This choice has a problematic consequence for a high-luminosity experiment: a non-zero crossing angle between the two beams involves a reduction of the luminosity, which is maximum for head-on collisions. This problem was solved with a particular technology called "crab cavities". A group of special radio-frequencies cavities capable to provide transverse fields was installed near the interaction point: its effect was to rotate the beam bounces and provide the head-on collision despite the finite crossing angle between the lines. Figure 2.2 illustrates how the crab cavities work and how they effects the bunches' orientation.

With this technology the total integrated luminosity delivered by the KEKB

(a) Finite angle collision

(b) Crab collision

Figure 2.2: The Crab cavities effect on colliding beam

reached in June 2010 the 1000 fb^{-1} (Fig. 2.4), 711 fb^{-1} were taken with $\sqrt{s} = 10.579$ GeV/c^2, while the remaining 289 fb^{-1} at the energies of the other bottomonia states, obtaining the world largest sample of $\Upsilon(1S)$, $\Upsilon(2S)$ and $\Upsilon(5S)$ (Fig. 2.3).

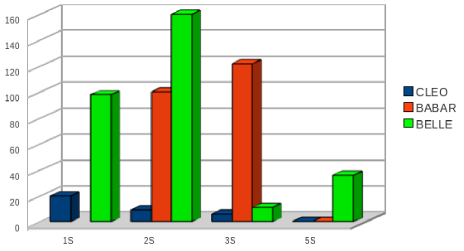

Figure 2.3: Number of events collected by BaBar, Belle and CLEO in the narrow bottomonium and $\Upsilon(5S)$ region. Counts are expressed millions.

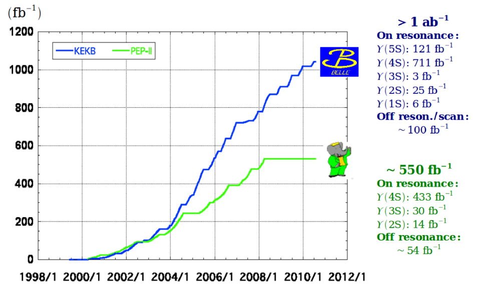

Figure 2.4: Total integrated luminosity delivered to the Belle experiment, compared to the BaBar performances.

2.3 The Belle Detector

One of the primary goals of the Belle experiment (Fig. 2.5)was the study of weak interactions, together with the oscillation in $B\bar{B}$ mesons' system. Both those objectives can be reached studying the B mesons coming for the $\Upsilon(4S)$ decay, thus the whole apparatus was optimized for the detection of particles with a momentum below 1 GeV/c, which is the typical range for particles coming from the B mesons decays. This constrain is crucial in the design of particle ID detectors, in particular for Cerenkov counters which have an intrinsic detection threshold, time of flight detectors, and drift chambers. Furthermore the study of B oscillation and Time-dependent CP violation requires a very precise determination of vertices's displaced

from the interaction point, requiring a radiation hard vertex detector capable to provide high resolution measurements [14].
The sub-detectors, arranged in a cylindrical shape, were:

- Silicon Vertex Detector (SVD), a tree-layer silicon strip detector placed near the interaction point,
- Central Drift Chamber (CDC) that provided the main tracking features.
- Time Of Flight (TOF) made with two layers of fast scintillators used in the particle-ID.
- Aerogel Cerenkov detector (ACC) used for particle ID.
- Electromagnetic calorimeter (ECL), a NaI(Tl) calorimeter.
- Kaon-Muon Detector (KLM), a system of RPC included in the the iron return joke of the magnet, used in muons and K_L reconstruction.

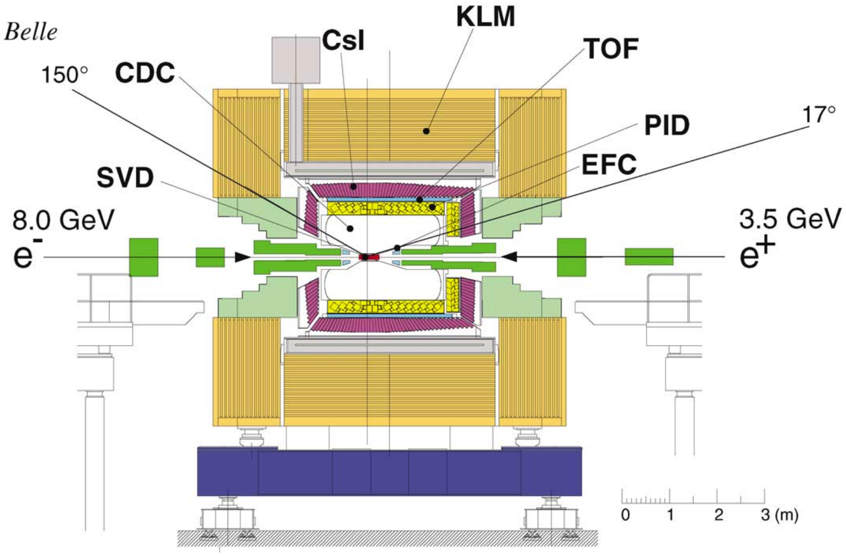

Figure 2.5: Belle detector layout

In this chapter the main characteristics of the different sub-detectors will be briefly discussed.

2.3.1 Silicon Vertex Detector

The inner silicon tracking system (SVD, Fig. 2.6) consisted in three layers of double sided strip detectors with a coverage of the 86% of the full solid angle and resolution along the beam axis of $100\mu m$. The main SVD feature was to identify displaced vertex and providing precise tracking information in order to improve the reconstruction performed with the central tracking system.

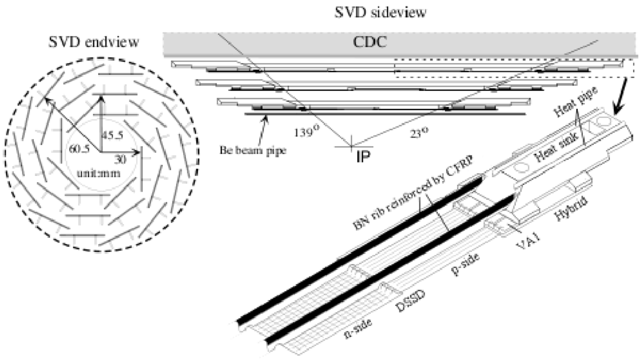

Figure 2.6: The Belle silicon vertex detector

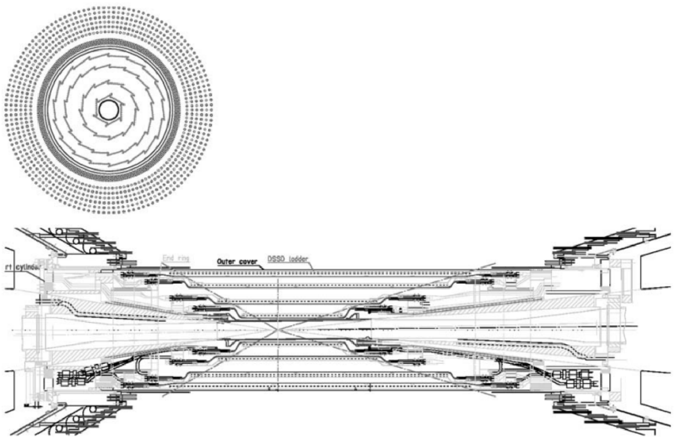

Figure 2.7: Upgraded SVD layout

The reconstruction of displaced vertexes is not a critical issue in the study of the $\Upsilon(2S) \rightarrow \Upsilon(1S)\eta$ transition since the decay time of the involved particle is small enough to make all the tracks to come directly from the interaction point. Nevertheless the contribution of the SVD in the charged tracks' momentum and impact parameter (i.e the distance between the track and the IP) reconstruction is not negligible. The impact parameter, in particular, is used in order to distinguish between charged tracks coming from the primary vertex, tracks due to conversion of photons in the detector and ghost tracks due to residual signals in the drift chamber. The SVD was updated two times: the first update consisted in minor changes in the data acquisition system (this layout has been called SVD 1.5), while during the final phase of the experiment the SVD was entirely replace with a new, 4-layers pixel-strip hybrid detector (Fig 2.7). This change has improved the tracking performances, also thanks to the reduced radius of the inner layer.

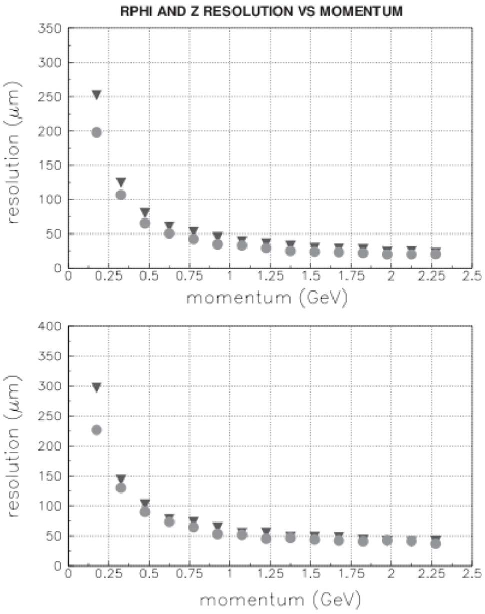

Figure 2.8: SVD performances in impact parameter measure. Top: z-axis direction; Bottom: xy plane. The triangles (circles) represent the resolution obtained with SVD 1.5 (2.0).

The performance in the impact parameter reconstruction is a function of the pseudo-momentum of the track, for both the z direction and the xy plane, as shown in Figure 2.8. A great improvement in the impact parameter resolution has been archived in the low momentum region with the second update, where pions coming from η decay can be found. The whole data sample recorded at the energy of the $\Upsilon(2S)$ resonance has been acquired with the SVD 2.0 fully operational.

2.3.2 Central Drift Chamber

The Central Drift Chamber (CDC) was a multi-wire drift chamber and represented the main tracking system. It consisted in a gas-filled chamber equipped with 50 layers containing from three to six axial or stereo layers and three cathode strip layers each one. In order to maximize the acceptance the CDC structure was asymmetric (Fig. 2.9), with a conical shape studied to keep the detector as close as possible to the interaction point. This features granted the reconstruction of low momentum tracks, such the pions coming from $\Upsilon(2S) \rightarrow \pi^+\pi^-\Upsilon(1S)$ transitions. Assuming a magnetic field of 1.5 T, the CDC's inner radius of 103.55 mm allowed the tracking of charged particles with transverse momentum greater than 50 MeV/c

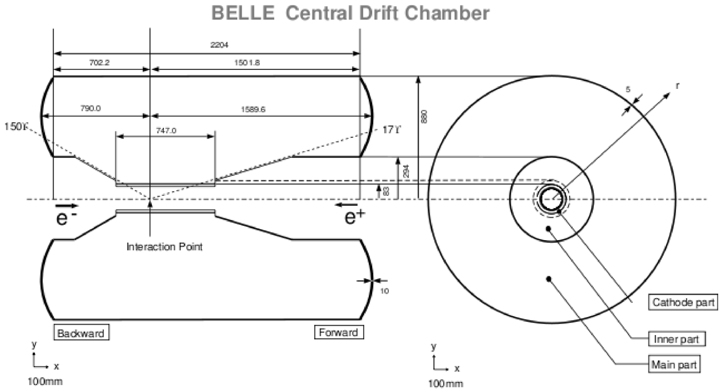

Figure 2.9: The Belle CDC

The gas melange was chosen in order to minimize the coulomb scattering and the radiation absorption: the chosen 50% helium - 50% ethane mixture offered a long radiation length (640 m) and a velocity drift that saturates at the value of 4 $cm/\mu m$ with an electric field of 1.6 $kV/(cm \cdot atm)$.

The momentum resolution of the CDC has been measured with cosmic rays, obtaining the distribution shown in figure 2.10. The region containing particles of particular interest for the analysis discussed in this thesis are marked. The large ethane component provided a good dE/dx resolution (Fig. 2.11), estimated with beam tests to be 5.2% for 3.5 GeV/c pions. The dE/dx information contributes to the likelihoods used for the particle identification.

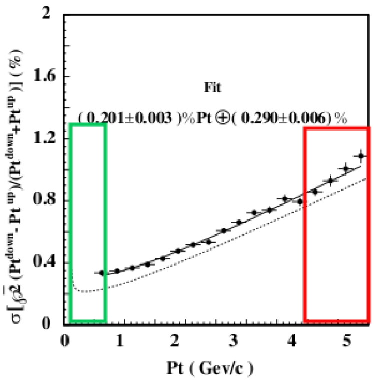

Figure 2.10: The CDC performances in momentum measurement. The red (green) box highlights the region were the tracks from $\Upsilon(1S)$ (η) decay can be found.

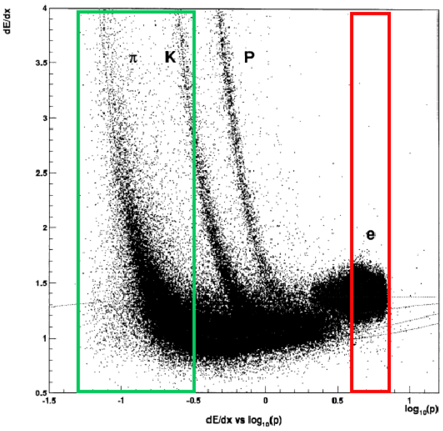

Figure 2.11: The CDC dE/dx resolution. The red (green) box highlights the region were the tracks from $\Upsilon(1S)$ (η) decay can be found.

2.3.3 Aerogel counter and Time of flight detector

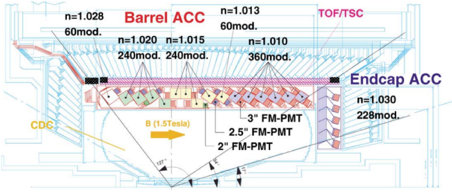

Figure 2.12: The Belle Aerogel counter.

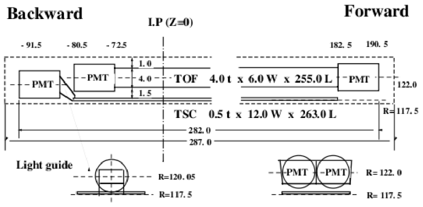

Figure 2.13: The Belle Time of Flight detector.

An Aerogel Cerenkov Counter System (ACC) and a Time Of Flight detector (TOF) were placed between the CDC and the electromagnetic calorimeter, as shown in Figure 2.12. The ACC system, consisting in 960 modules of hydrophobic aerogel with refraction index between 1.01 and 1.03, was optimized in order to separate kaons from pions in the range not covered by the dE/dx information.

The TOF consisted in a 4 cm thick fast scintillator layer, with a time resolution of 100 ps for particle with momentum below 1.2 GeV/c. A layer of 0.5 cm thick scintillator (TSC) was used as coincidence system in order to avoid noise from accidental counts (Fig. 2.13). The TOF system is used as part of the trigger system for the other subsystems.

The inner radius of the ACC was 0.880 m, so only particles with transverse momentum $p_t > 398$ MeV/c could reach this section of the detector. This feature makes the ACC and the TOF less important than the tracking system in the $\Upsilon(2S) \to \Upsilon(1S)\eta$ analysis, since the decay product of the η can not reach them and the leptons from the $\Upsilon(1S)$ have a typical momentum that exceeds the limits imposed by the TOF resolution.

2.3.4 The electromagnetic calorimeter

The Belle Electromagnetic Calorimeter (ECL) was divided into three sections, the barrel and the two endcaps ("forward" and "backward" with respect to the HER beam direction). The total coverage is 91% of the solid angle, with a 3% of acceptance loss due to the gaps between barrel and endcaps that provides the pathway for the cabling system of the inner detectors. The ECL consisted in 8736 CsI(Tl) crystals with a typicaldimension of (55x55)mm on the front face and 30 cm of depth, correspondespoding to 16.2 radiation lengths, arranged to point approximately to the interaction point (Fig. 2.14) . The size of the crystals was arranged in such a way that approximately the 80% of the total energy of a photon injected in its center remained contained in the crystal. The energy resolution studies were performed with electrons and photon beams, using 3x3 (Fig. 2.16) and 5x5 (Fig. 2.15) crystal blocks.

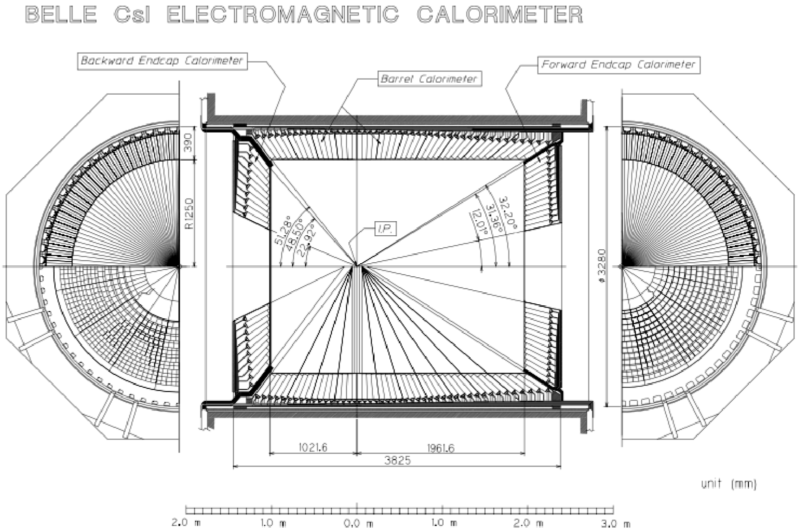

Figure 2.14: The Belle Calorimeter

The energy resolution shape can be fitted with the quadratic sum of three terms obtaining, for a 5x5 block:

$$\frac{\sigma_E}{E} = \frac{0.0066(\%)}{E} + \frac{1.53(\%)}{E^{(}1/4)} + 1.18(\%).$$

For a 3x3 block the parameters are different but the functional form is the same:

$$\frac{\sigma_E}{E} = \frac{0.066(\%)}{E} + \frac{0.81(\%)}{E^{(}1/4)} + 1.34(\%)$$

The photon reconstruction algorithm uses both the 5X5 and 3X3 block information.

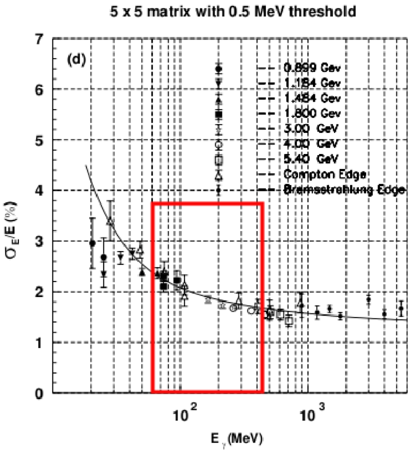

Figure 2.15: ECL energy resolution using a 5x5 block of crystals

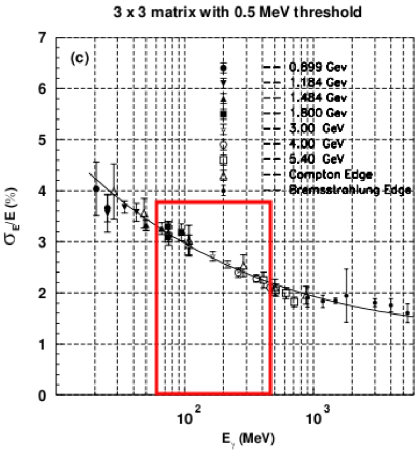

Figure 2.16: ECL energy resolution using a 3x3 block of crystals

The ECL resolution in measuring the invariant mass of photon pairs is a crucial feature in the study of transitions involving the η reconstruction. Figures 2.17 and 2.18 show the invariant mass distribution of reconstructed π^0's and η's in hadronic events, where the photon energy is required to be greater than 30 MeV/c^2.

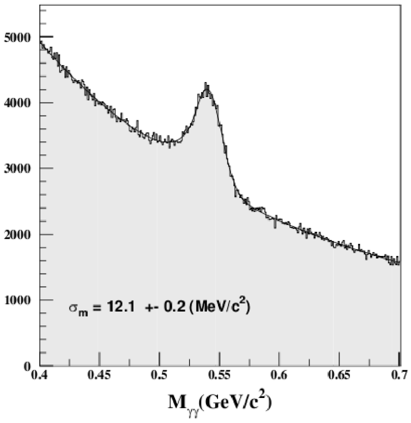

Figure 2.17: $\gamma\gamma$ pairs invariant mass in the η region, from hadronic events

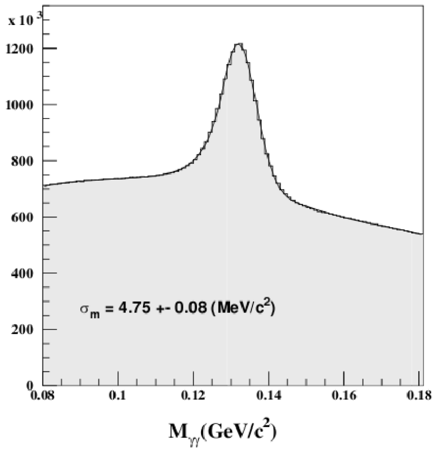

Figure 2.18: $\gamma\gamma$ pairs invariant mass in the π^0 region, from hadronic events

2.3.5 Kaons and Muons detection system

The KML consists in alternating layers of charged particles detectors and 4.7 *cm*-thick iron plates, with a total absorption length or 3.9 interaction lengths.
The detection of charged particles is provided by a glass-electrode-resistive plate chambers, arranged in double layers called super-layers as shown in figure 2.19.

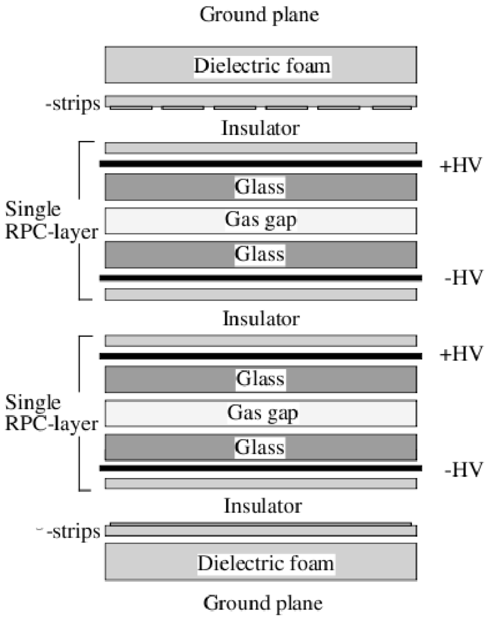

Figure 2.19: The Belle Kaon and Muon detector

The KLM performances in muon detection were studied with cosmic rays with momentum greater than 500 MeV/c, since particles with lower momentum produced in the IP can not reach the KLM due to the presence of the 1.5 T magnetic field. In figure 2.21 is shown the measured efficiency as function of the muon momentum, while fig. 2.20 shows the rake rate due to μ/π misidentification. The pions were selected from $K_s \to \pi^+\pi^-$ events in e^+e^- collisions. For muon with momentum above 1.5 GeV/c the identification efficiency is over 90% and the fake rate is less than 5%.

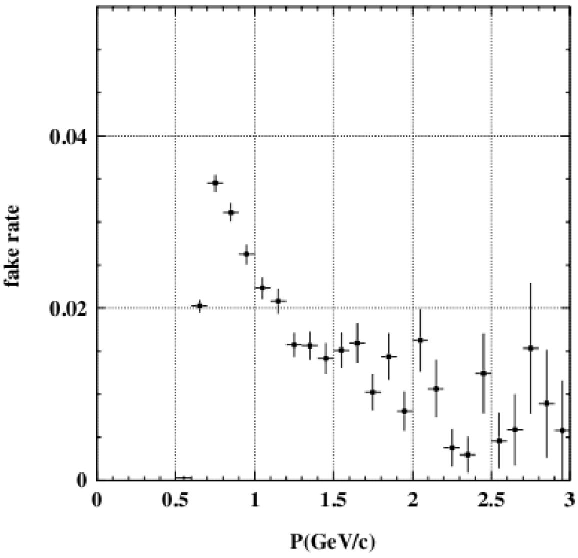

Figure 2.20: Muon identification fake rate

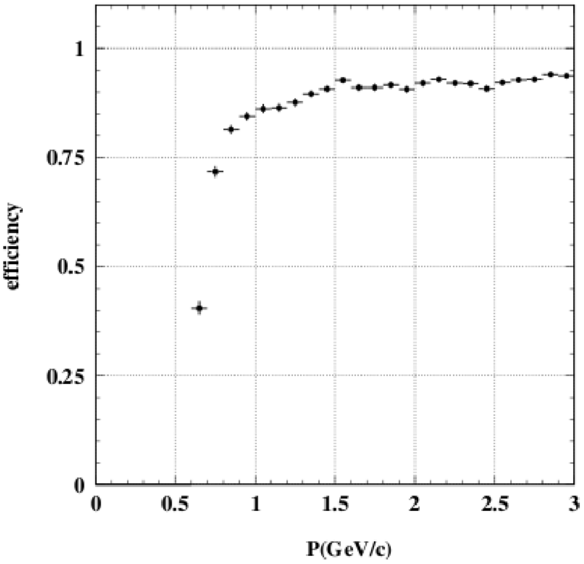

Figure 2.21: Muon detection efficiency

Chapter 3

Montecarlo studies and selection criteria

In this chapter the Montecarlo (MC) studies conducted on the $\Upsilon(2S) \to \eta\Upsilon(1S)$ transition will be presented: a full Montecarlo simulation of all the resonant backgrounds has been made specifically for this analysis, and the selection criteria were fully optimized using these MC samples and then applied to the data sample, in order to perform a completely blind analysis.

Since none of the available standard skims provided by the Belle collaboration was adequate for this analysis, we started from the unskimmed data samples and we designed a suitable skim criteria. This selection, based on the high momentum tracks characteristics, is applied to the full $\Upsilon(2S)$ sample in order select only events with a candidate $\Upsilon(1S) \to e^+e^-, \mu^+\mu^-$ in the final state. After the skim selection we required tracks and calorimeter clusters to meet some quality condition in order to reject both ghost tracks in CDC and noisy rechits in the ECL. In order to improve the resolution on the reconstructed $\Upsilon(1S)$, a dedicated selection is devoted to the reconstruction of the photons irradiated by the high momentum leptons resulting from the decay of $\Upsilon(1S)$ itself. All the γ, π, e and μ that satisfied these cuts represents the candidates for the final event reconstruction. Therefore two kinematic fits will be applied: the first one in order to constrain the two leptons and the photons tagged as radiative ones to have the invariant mass of the $\Upsilon(1S)$, the second to constrain the $\Upsilon(1S)$ candidate obtained from the first fit and the η candidate to have the invariant mass of the $\Upsilon(2S)$. After this procedure, a final selection is made with different conditions, according to the η and the $\Upsilon(1S)$ decay mode under investigation, in order to reject the residual background. The η candidate mass has been chosen as variable for the final fit and branching ratio calculation, so all the cuts has been performed, when possible, on observable weakly correlated with the η mass.

Every cut value has been optimized by maximizing the Figure of Merit:

$$FoM = \frac{N_{signal}}{\sqrt{N_{signal} + N_{background}}}.$$

3.1 Signal topology and background determination

The inclusive search for the $\Upsilon(2S) \to \eta\Upsilon(1S)$ transition requires the full reconstruction of all the involved particles.

The primary η decay modes are $\eta \to \gamma\gamma$, with branching fraction $\mathcal{B} = 39.31\%$, $\eta \to \pi^0\pi^0\pi^0$, with $\mathcal{B} = 32.57\%$, $\eta \to \pi^+\pi^-\pi^0$ with $\mathcal{B} = 22.74\%$ and $\eta \to \pi^+\pi^-\gamma$ with $\mathcal{B} = 4.60\%$.

In this analysis the η will be detected either in the $\gamma\gamma$ and $\pi^+\pi^-\pi^0$ modes. The $\pi^+\pi^-\gamma$ mode has been discarded due to its low branching ratio, while the high number of low energy photons due to the background related to the beam activity leads to the exclusion of the $3\pi^0$ mode. The $\Upsilon(1S)$ will be detected in the two leptonic modes $\Upsilon(1S) \to e^+e^-$ and $\Upsilon(1S) \to \mu^+\mu^-$. The branching ratio is $\mathcal{B} = 2.5\%$ for both those modes. All the final states resulting from the combination of these channels have a clean signature: with $\eta \to \pi^+\pi^-\pi^0$ we have to search for

- 2 high momentum tracks coming from $\Upsilon(1S)$ decay,
- 2 low momentum tracks coming from η decay,
- 2 low energy photons coming from π^0 decay,

while when detecting $\eta \to \gamma\gamma$ the signature is

- 2 high momentum tracks coming from $\Upsilon(1S)$ decay,
- 2 photons coming from η decay,
- no other charged tracks.

Two different kind of processes can provide large backgrounds: transitions (both hadronic and radiative) between $\Upsilon(2S)$ and $\Upsilon(1S)$ and non-resonant reactions from the continuum $e^+e^- \to q\bar{q} \to X$. In particular all the others major transitions between $\Upsilon(2S)$ and $\Upsilon(1S)$ represent a potential background source.
Resonant backgrounds for the $\pi^+\pi^-\pi^0$ mode from $\Upsilon(2S) \to \pi^+\pi^-\Upsilon(1S)$ and $\Upsilon(2S) \to \pi^0\pi^0\Upsilon(1S)$ are expected: both transitions have branching ratios which are 3 orders of magnitude larger than the searched one. In both cases, the final state can be easily confused with the signal final state:

- in the $\pi^+\pi^-\Upsilon(1S)$ case, a fake π^0 may be created combining photons from FSR, bremsstrahlung, or beam background.

- in the $\pi^0\pi^0\Upsilon(1S)$ case, one of the four photons may convert in the inner detector and create a low momentum electron-positron pair which is then wrongly tagged as charged $\pi^+\pi^-$ pair, while the other photon from the same π^0 escapes detection.

The $\eta \to \gamma\gamma$ mode may be contaminated by backgrounds with the same final state, not just on the resonance peak, but also in continuum:

- The double cascade transitions involving an intermediate χ_{bJ} state (i.e. $\Upsilon(2S) \to \gamma_1\chi_{bJ}(1P) \to \gamma_1\gamma_2\Upsilon(1S)$) to compete with the $\pi^0\pi^0\Upsilon(1S)$ transition, may represent source of background;

- The doubly radiative continuum process $e^+e^- \to (\mu^+\mu^-, e^+e^-)\gamma\gamma$ or singly radiative processes like Initial State Radiation (ISR), Final State Radiation (FSR) or radiative Bhabha scattering, with an accidental extra photon coming from the beam activity are expected to represent a primary source of background.

The branching ratios of the background processes are summarize in table 3.1. The Belle experiment has collected, during the experiments 67 and 71, 158 ± 3.6 millions of $\Upsilon(2S)$. The total branching ratio, calculated including the $\Upsilon(1S) \to e^+e^-, \mu^+\mu^-$, the expected number of events for the signal and the background sources and the ratio $\frac{\mathcal{B}(signal)}{\mathcal{B}(background)}$ are reported in table 3.2

Table 3.1: Branching ratios

Process	Branching ratio	Note
$\Upsilon(2S) \to \eta\Upsilon(1S)$	$2 \cdot 10^{-4}$	CLEO[8]
$\Upsilon(2S) \to \pi^+\pi^-\Upsilon(1S)$	18.0%	CLEO [8]
$\Upsilon(2S) \to \pi^0\pi^0\Upsilon(1S)$	9.0%	assuming isospin symmetry
$\Upsilon(2S) \to \gamma\chi_{b0}(1P)$	3.8%	PDG[15]
$\Upsilon(2S) \to \gamma\chi_{b1}(1P)$	6.9%	PDG[15]
$\Upsilon(2S) \to \gamma\chi_{b2}(1P)$	7.15%	PDG[15]
$\Upsilon(1S) \to e^+e^-, \mu^+\mu^-$	2.48%	PDG[15]
$\eta \to \pi^+\pi^-\pi^0$	22.74%	PDG[15]
$\eta \to \gamma\gamma$	39.31%	PDG[15]
$\chi_{b0} \to \gamma\Upsilon(1S)$	6%	upper limit PDG[15]
$\chi_{b1} \to \gamma\Upsilon(1S)$	35%	PDG[15]
$\chi_{b2} \to \gamma\Upsilon(1S)$	22%	PDG[15]

3.2 Data samples

In December 2008, Belle took a first set of data at $\Upsilon(2S)$ energy, during experiment 67. A brief scan was used to find the resonance peak. After establishing the energy settings, 6.5 fb^{-1} data were taken only on 2S peak. The total $\Upsilon(2S)$ yield, 46.4±1.5 Millions, was calculated from the number of $\pi^+\pi^-\mu^+\mu^-$ events. The product of decay ratios $\mathcal{B}(\Upsilon(2S) \to \pi^+\pi^-\Upsilon(1S)) \times \mathcal{B}(\Upsilon(1S) \to \mu^+\mu^-)$=0.449±0.013% (known with 3.3% relative error), taken from PDG, was used, and dominates the systematic error on 2S yield. By using the $\pi^+\pi^-e^+e^-$ events, N($\Upsilon(2S)$)=45.9±2.3 Millions is obtained. A second sample of 2S decays was integrated in November 2009, Exp.71. In between two periods of data taking on 2S peak, a sample of data on continuum, 30 MeV below the 2S energy, was accumulated. Table 3.3 summarizes all the essential information on these datasets. The total sample of 2S data amounts to 157.8±3.6 Millions decays, which represents the world's largest sample to date (Babar, with 100 Millions, has the second largest).

Table 3.2: Total branching ratios, expected counts in 158 Millions of $\Upsilon(2S)$ decays the ratio S/B between the expected signal yield background yield for each transition analyzed in this work.

Channel	BR	Counts	S/B ratio
$\Upsilon(2S) \to \Upsilon(1S)\eta(\to \gamma\gamma)$	$3.93 \cdot 10^{-6}$	628	-
$\Upsilon(2S) \to \Upsilon(1S)\eta(\to \pi^+\pi^-\pi^0)$	$2.27 \cdot 10^{-6}$	363	-
$\Upsilon(2S) \to \pi^+\pi^-\Upsilon(1S)$	0.9%	1.44 Millions	$2.5 \cdot 10^{-4}$
$\Upsilon(2S) \to \pi^0\pi^0\Upsilon(1S)$	0.45%	0.72 Millions	$5.0 \cdot 10^{-4}$
$\Upsilon(2S) \to \gamma\chi_{b2} \to \gamma\gamma\Upsilon(1S)$	$7.8 \cdot 10^{-4}$	0.125 Millions	$5.01 \cdot 10^{-3}$
$\Upsilon(2S) \to \gamma\chi_{b1} \to \gamma\gamma\Upsilon(1S)$	$1.2 \cdot 10^{-3}$	0.193 Millions	$3.26 \cdot 10^{-3}$
$\Upsilon(2S) \to \gamma\chi_{b0} \to \gamma\gamma\Upsilon(1S)$	$1.4 \cdot 10^{-4}$	0.018 Millions	$3.45 \cdot 10^{-2}$

Table 3.3: Data samples taken in the proximity of $\Upsilon(2S)$.

dataset	$\sqrt{s}(MeV)$	Exp.	runs	Ldt($1/pb$)	N(Υ)
$\Upsilon(2S)$ scan	10023.3 ±(30,6,4,2,0)	67	1002-1015	159	-
$\Upsilon(2S)$ peak	10023.3	67	1016-1123	6523	41.7M
$\Upsilon(2S)$ continuum	9993.3	71	498-536	1692	
$\Upsilon(2S)$ scan	10023.3 ±(1,3),+5 MeV	71	303-312	98	
$\Upsilon(2S)$ peak	10023.3	71	313-497,537-696	18177	116.1M

3.3 MonteCarlo samples

Within the blind analysis approach, a MC sample for each background source have been generated. In particular all the resonant backgrounds were generated using the EVTGEN package [16], while the detector simulation has been made with Geant4 with the default Belle configuration.

EVTGEN provides different modules to model the angular distribution and dalitz plots of the decays. The $\eta \to 3\pi$ decays were generated using the default module *ETA DALITZ* .

All $\Upsilon(2S) \to \eta\Upsilon(1S)$ has been studied and generated with module '*HELAMP* ' and parameters set to '1 0 0 0 -1 0'. The HELAMP parameters represent the helicity amplitudes of the transition.

The $\Upsilon(2S) \to \pi\pi\Upsilon(1S)$ decay is modeled using the default model *VVPIPI*, modified setting parameter $\lambda = 0.28$, in order to fit more accurately the dipion mass distribution. The λ parameter represents the coefficient of the m_π related term in the DiPion mass distribution which is expected to be $\frac{d\Gamma}{dm_{\pi\pi}} \propto (m_{\pi\pi}^2 - \lambda m_\pi^2)^2$. The $\Upsilon(1S) \to$ dilepton decays are modeled using the standard EvtGen package for a vector state decaying into two leptons *VLL* .

PHOTOS is the standard package to simulate the final state radiation processes; it has been used for both $\Upsilon(1S)$ and $\eta \to 3\pi$ decays.

Concerning the transitions with χ_{bj} intermediate states, they have been modeled using the helicity amplitudes expected in dipole approximation:

- *HELAMP* with parameters '1 0 1 0' for the $\Upsilon(2S) \to \gamma\chi_{b0}$ transition, and for the $\chi_{b0} \to \gamma\Upsilon(1S)$;
- *HELAMP* with parameters '1 0 1 0 -1 0 -1 0' for both $\Upsilon(2S) \to \gamma\chi_{b1}$ and $\chi_{b1} \to \gamma\Upsilon(1S)$;
- *HELAMP* with parameters '2.494897 0 1.7320508 0 1 0 1 0 1.7320508 0 2.494897' for the $\Upsilon(2S) \to \gamma\chi_{b2}$ transition, and a flat phase space distribution (module *PHSP*) for the $\chi_{b2} \to \gamma\Upsilon(1S)$, since a known bug prevents running EvtGen for the double cascades with a large number of independent amplitudes.

Sizes and other infos on these samples are summarized in table 3.4.

Table 3.4: MonteCarlo data samples generated for the optimization of selection cuts.

$\Upsilon(2S)$ Decay channel	$\sqrt{s}(MeV)$	N. Events
$\Upsilon \to \mu^+\mu^-; \eta \to \pi^+\pi^-\pi^0$	10023.3	0.5M
$\Upsilon \to e^+e^-; \eta \to \pi^+\pi^-\pi^0$	10023.3	0.5M
$\Upsilon \to \mu^+\mu^-; \eta \to \gamma\gamma$	10023.3	0.17M
$\Upsilon \to e^+e^-; \eta \to \gamma\gamma$	10023.3	0.17M
$\Upsilon\pi^+\pi^-; \Upsilon \to \mu^+\mu^-$	10023.3	2.2M
$\Upsilon\pi^+\pi^-; \Upsilon \to e^+e^-$	10023.3	2.2M
$\Upsilon\pi^0\pi^0; \Upsilon \to \mu^+\mu^-$	10023.3	1.1M
$\Upsilon\pi^0\pi^0; \Upsilon \to e^+e^-$	10023.3	1.1M
$\chi_{b0}\gamma \to \Upsilon\gamma\gamma; \Upsilon \to \mu^+\mu^-$	10023.3	70K
$\chi_{b0}\gamma \to \Upsilon\gamma\gamma; \Upsilon \to e^+e^-$	10023.3	70K
$\chi_{b1}\gamma \to \Upsilon\gamma\gamma; \Upsilon \to \mu^+\mu^-$	10023.3	0.6M
$\chi_{b1}\gamma \to \Upsilon\gamma\gamma; \Upsilon \to e^+e^-$	10023.3	0.6M
$\chi_{b2}\gamma \to \Upsilon\gamma\gamma; \Upsilon \to \mu^+\mu^-$	10023.3	0.4M
$\chi_{b2}\gamma \to \Upsilon\gamma\gamma; \Upsilon \to e^+e^-$	10023.3	0.4M

The EVTGEN and Geant4 simulation is still not enough accurate to be used in the optimization procedure of the selection criteria: other contributions coming from the beam activities or particular environmental issues that may change run by run can not be properly simulated, but can have a major impact in the search for low statistic channels.

To partially solve this problem some random triggered events were recorded during the data taking. Those events can be added to the generated montecarlo events to account for realistic background conditions, as accidental photons that are likely to contribute fake events with similar topologies, when overlapped to radiative QED processes.

The background from continuum processes has been primarily analyzed using the $1.71fb^{-1}$ sample of data taken 30 MeV below the $\Upsilon(2S)$ energy and a small sample of radiative bhabha scattering events $e^+e^- \to \mu^+\mu^-, e^+e^- + n\gamma$.

3.4 The preliminary selection and the definition of γ, $\pi^{\pm}$ and leptons candidates.

3.4.1 Skimming condition

The first step in the analysis is the selection of the events with an $\Upsilon(1S) \rightarrow e^+e^-, \mu^+\mu^-$ candidate in the final state.

A preliminary selection criteria, called StiffPairSkim, has been prepared selecting only events with two high momentum tracks ($p^* > 4$ GeV/c) with opposite charge, with no further cuts on particle identification.

Those tracks are the candidate leptons coming form the $\Upsilon(1S)$ decay, which are expected to have, neglecting the lepton mass and the $\Upsilon(1S)$ momentum, $p^* = 4.730$ GeV/c.

In figure 3.1 is shown the momentum spectrum of charged tracks in $\eta \rightarrow \pi^+\pi^-\pi^0, \Upsilon(1S) \rightarrow ee, \mu\mu$ montecarlo events. The low momentum region ($p^* > 1$ GeV/c) contains the tracks coming from the η decay, while in the high momentum region ($p^* > 4$ GeV/c) the peak due to the leptons from the $\Upsilon(1S)$ decay is clearly visible. The intermediate region is populated mainly by bad reconstructed e^+ or e^-.

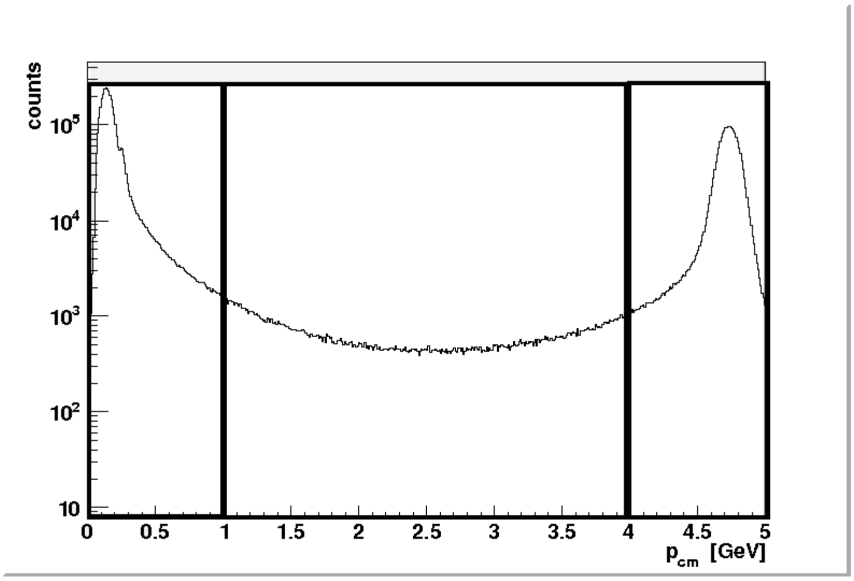

Figure 3.1: Charged Track spectrum in $\eta \rightarrow \pi^+\pi^-\pi^0$ montecarlo events. The three momentum regions (high, medium and low) are marked

The StiffPairSkim cut is meant to allow a good normalization of the feed-down from QED backgrounds such as radiative Bhabha, and $\mu^+\mu^-\gamma$, which are expected to play a major role in the search for $\eta \to \gamma\gamma$ mode. Concerning $\eta \to \pi^+\pi^-\pi^0$, QED backgrounds are unlikely to produce dileptons associated simultaneously to two extra charged tracks and a π^0 candidate. In addition, the continuum events from hadronic channels may hardly contribute dileptons at such high energy.

The StiffPairSkim from the $1.71 fb^{-1}$ continuum data set contains 7.963 Million events corresponding to an effective cross section of $\sigma_{SP,cont} = N_{events}/Ł_{cont} = 4.68 nb$, from which one can estimate a background of 113 M continuum events on the peak data.
This means that the continuum background will be studied with a sample that is $\approx$ 7% of the total expected yield, while resonant backgrounds with samples $\approx$ 4 times the expected yield.

The skimming efficiency, defined as the fraction of the total dataset which survives the above mentioned cut, is $\epsilon(StiffPair) = 15\%$. The nature of the events selected by the StiffPairSkim condition can be studied using the Kinetic Boundary parameter (KB) and the mass of the DiLepton. The $KB = p^*(ll) - 0.5 \cdot \frac{M^2(ll)-s}{\sqrt{s}}$ represents the distance from the Kinematic Boundary, i.e. the maximum CM momentum that a dilepton with mass $M(ll)$ can reach, at a given value of $\sqrt{s}$. Neglecting the experimental resolution, physical values for KB are lower than zero. The red circles in 3.2 and 3.3 indicates the $\Upsilon(1S)$ region, visible in the $\mu\mu$ channel, which is less affected

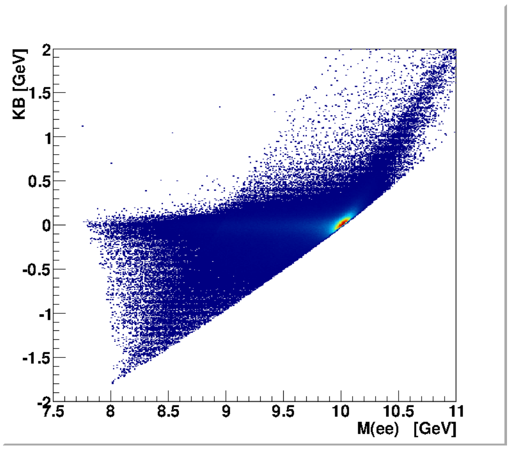

Figure 3.2: KB versus $M(e^+e^-)$, exp67 data

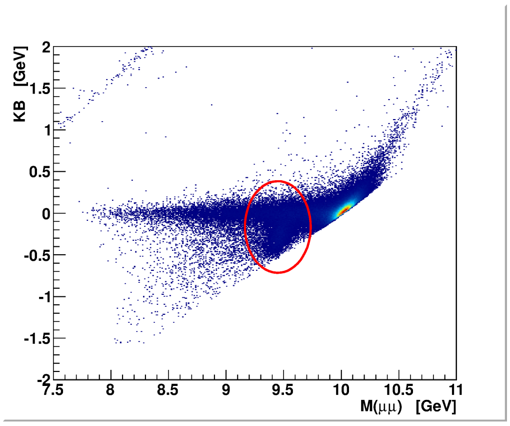

Figure 3.3: KB versus $M(\mu^+\mu^-)$, exp67 data

by QED backgrounds. The tail at $KB = 0$ is filled by events where the dilepton bounces off a photon, i.e. radiative return (ISR) or final state radiation (FSR). After the loose cut represented by the skimming condition, a set of cuts has been applied on the single charged and neutral entities reconstructed. The aim of those cut is the rejection of the fake tracks, noisy clusters or final state radiation photons that can contribute to create multiple η candidate. The impact of those processes can be see in the multiplicity of neutral and charged entities in signal montecarlo events. For $\eta \rightarrow 3\pi$ events two low momentum tracks, two high momentum tracks and one π^0 candidate are expected. Figures 3.4 and 3.5 show the multiplicities measured in montecarlo signal events after the skimming cuts were applied.

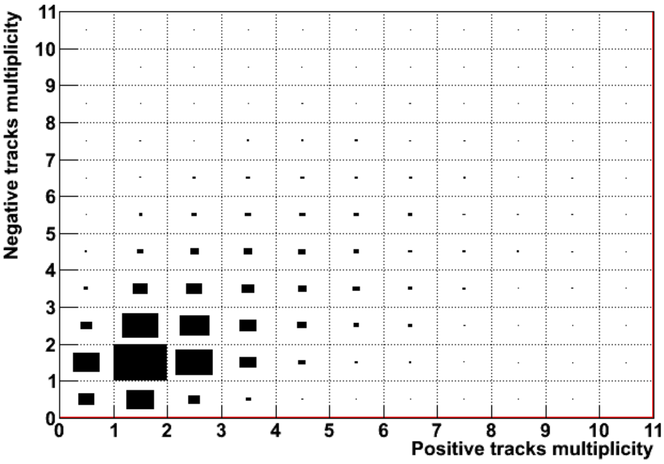

Figure 3.4: Number of low momentum positive tracks compared to the number of negative tracks, in $\eta \rightarrow 3\pi$ montecarlo events

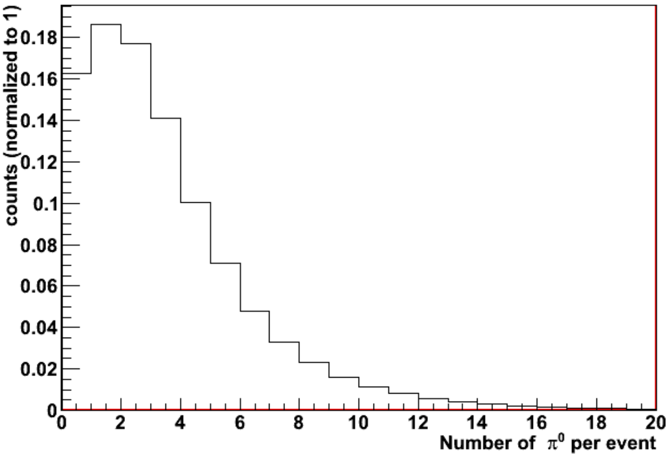

Figure 3.5: Number of π^0 candidates in $\eta \to 3\pi$ montecarlo events

3.4.2 Low Momentum tracks: PID and quality selection.

The Belle particle identification system is based on the definition of different standard likelihood functions. The user can customize these functions by including or excluding the information from each sub-detector according to the analysis requirements. The standard likelihood functions that can be profitably used in this analysis are L_μ, the likelihood function for the muon hypothesis, p_e which is the electron probability, defined as the ratio between the likelihood for the electron hypothesis L_e and the hadronic hypothesis L_{had} ($p_e = \frac{L_e}{L_e+L_{had}}$) and L_e itself, which is particularly useful in distinguishing electrons from pions.

During the analysis we found that all the possible particle-ID algorithm had poor performances in the low momentum region, where the pions coming from the η decay can be found. Since this problem is related to the very poor particle ID efficiency of the default likelihoods in this region is (Fig. 3.6), we decided not to try to perform any identification on the low momentum tracks, that are all tagged as pions.

Only 26.56% of signal events with $\eta \to \pi^+\pi^-\pi^0$ exhibits exactly two low momentum tracks ($p^* < 1$ GeV/c) of opposite charge, while 57.74 % has greater multiplicity, up to 10 tracks of both signs; this behavior is mainly due to fake and ghost tracks in the CDC.

Since the real $\pi^{\pm}$ must come from the primary vertex, the low momentum tracks

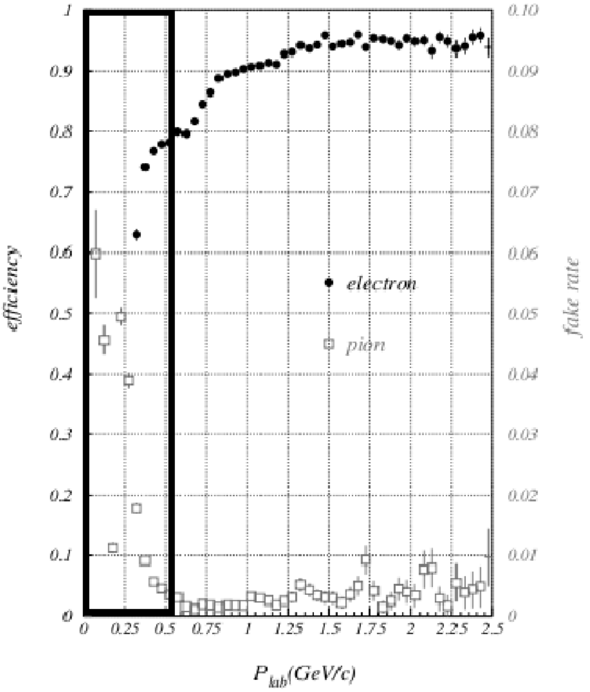

Figure 3.6: The standard efficiency in e identification as function of the particle momentum. The squares represent the e/π fake rate. The box remarks the region where the pions coming from the η decay can be found

are required to have to have impact parameters $|\Delta z| < 3.0\ cm$ and $|\Delta r| < 0.5\ cm$. The impact parameters are the minimum approach distance between the track and the nominal interaction point measured in the xy plane (Δr) and along the z axis (Δz).

Fig.3.7 and 3.8 show the impact parameters distribution for both real π and ghost tracks in signal events. The effect on the number of low momentum tracks of the selection is shown in Fig.3.9 and 3.10

Table 3.5 summarizes the performance of the impact parameter cuts on ghost tracks rejection. $N(fake\ \pi)/N(real\ \pi)$ represents the ratio between the mean number of fake tracks and the mean number of real tracks per event in signal montecarlo.

Table 3.5: Ghost tracks rejection performances.

Ratio	without cuts	with cuts
$N(fake\ \pi^-)/N(real\ \pi^-)$	0.810	0.030
$N(fake\ \pi^+)/N(real\ \pi^+)$	0.874	0.036

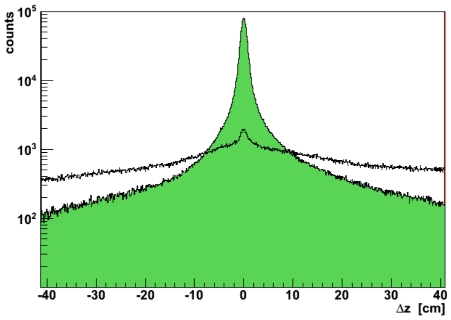

Figure 3.7: $|\Delta z|$ for real π and fake tracks in signal events.

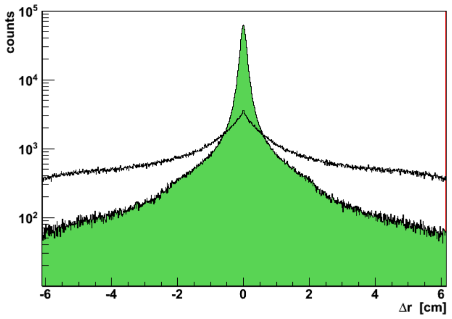

Figure 3.8: $|\Delta r|$ for real π and fake tracks in signal events.

3.4.3 High Momentum leptons: PID and quality selection.

The StiffPairSkim criterion rejects all the non $\Upsilon(1S)$-like final states, but does not effects the yield coming from the elastic peak at the the $\Upsilon(2S)$ energy, namely the peak resulting from the non-radiative Bhabha scattering.
A request on the invariant mass of the lepton pair is ideal in order to rejects those events, but requires the identification of the two leptons.
Concerning the leptons, the default likelihood functions can be used but they must be adapted to to this particular analysis. The information from the TOF and the Cerenkov counter are removed from the Likelihood definition since the $\Upsilon(1S)$ decay products have a typical momentum that is far above the detectors' capability.
The primary source of information for the particle ID remains the ratio $R_{ECL} = E_{ECL}/p$, where E_{ECL} is the energy deposited in the calorimeter by the particle and p is the magnitude of its momentum in the laboratory frame, measured by the tracking system. This ratio is expected to be $R_{ECL} << 1$ for muons and $R_{ECL} \approx 1$ for electrons.

The R_{ECL} ratio has been studied as function of the position of the ECL cluster to

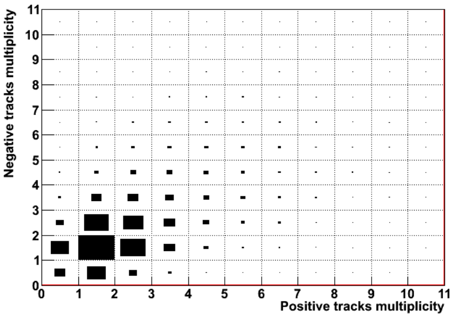

Figure 3.9: Low momentum tracks: N^+ vs N^- without cut.

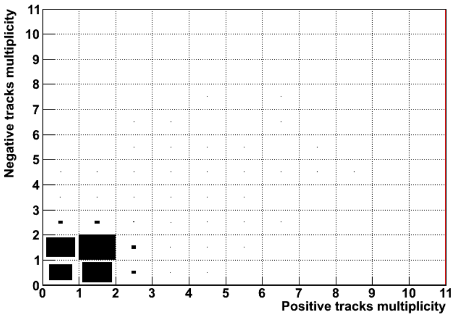

Figure 3.10: Low momentum tracks: N^+ vs N^- with cut on Δz at 3.0 cm and Δr at 0.5 cm.

investigate the possibility of impose some acceptance cut and improve the likelihood-based particle ID, or even avoid it using directly the ECL signal. Figure 3.11 and 3.12 shows the R_{ECL} measured in montecarlo events.

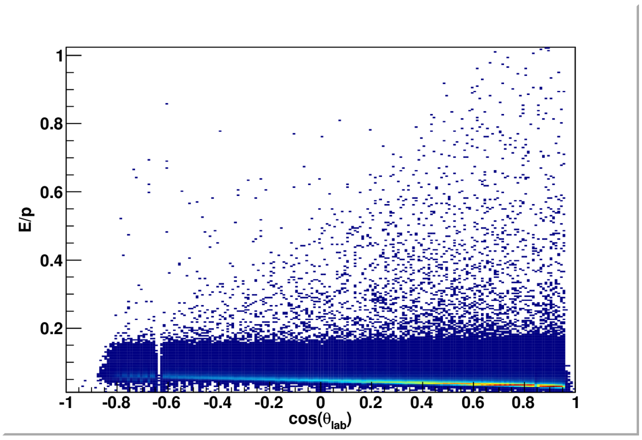

Figure 3.11: Muon E_{ECL}/p in montecarlo events as function of the polar angle of the incident track.

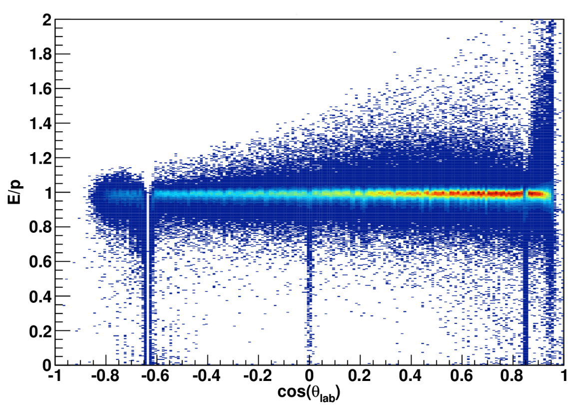

Figure 3.12: Electron E_{ECL}/p in montecarlo events as function of the polar angle of the incident track.

In figure 3.12 it's clearly visible the junction between the endcaps and the barrel regions, together with the barrel junction at $\theta = \pi/2$. The optimization of the R_{ECL} measurement requires the exclusion of the forward endcap region, with a $\approx 30\%$ loose of efficiency in signal events. In order to keep the reconstruction efficiency as high as possible, no acceptance cuts has been imposed, and the identification of the lepton has been made with the Likelihood functions, deprived of the TOF and ACC information.

A tracks is then labeled as leptons if at least one of these two conditions is satisfied:

- $L_{mu} > L_{\mu,cut}$;
- $p = L_e/(L_e + L_{had})$ is above p_{cut}.

Four different cuts values for p_{cut} and $L_{\mu,cut}$ have been studied: 0.1, 0.2, 0.6, and 0.8, as suggested by the Belle Particle Identification Group. The cut value of 0.2 has been chosen for both electrons ad muons.

If a track has both p and L_μ greater than the cut level, then it is identified as electron or muon according to which value is larger: if $L_\mu > p$ the identification is muon, else electron.

The misidentification rate for the single track is $1.5 \cdot 10^{-5}$ for both e and μ. After the particle ID definition other simple request can applied on the leptons:

- $9.0 < M(ll) < 9.8$: the Di-Lepton must have invariant mass in the $\Upsilon(1S)$ region

- The two leptons must have the same particle ID.

3.4.4 Photons: quality cuts and final state radiation reconstruction

Final state radiation photons or photons from bremsstrahlung are responsible for a bad $\Upsilon(1S)$ invariant mass and momentum reconstruction and increase the combinatorial background in the η and π^0 reconstruction. Furthermore the reconstruction of final state radiation photons reduces the background from doubly or single radiative bhabha events, which is expected to be a large background source while detecting $\eta \to \gamma\gamma$

Since the radiative photons are emitted primary along the direction of emitting lepton's momentum, an ECL cluster is tagged as FSR photon if it lays in a cone of 200 mrad from a high momentum tracks. The momentum of these photons will be then added to the lepton momentum in the $\Upsilon(1S)$ reconstruction phase.

The selected opening angle allows to keep the percentage of photons from $\eta \to \gamma\gamma$ decay tagged as final state radiation under 2%

Table 3.6 shows the tagging efficiency of this criterion, calculated using the montecarlo truth information. The efficiency is lower in the electron case than the muon case since the electromagnetic shower created by an electron have a larger shape than the one created by a muon; this means that the ECL clusters due to final state radiation may be easily included in the electron shower, while this doesn't happen for the muons, since a more compact shower allows the reconstruction of separated clusters near the track direction.

Table 3.6: Final state radiation selection efficiencies.

Photon source	Lepton	Selected fraction
Signal	e	1.1%
Signal	μ	1.57%
Final state Radiation	e	17.23%
Final state Radiation	μ	27.69%
Bremsstrahlung	e	6.54%
Bremsstrahlung	μ	3.18%

The remaining neutral entities reconstructed in the calorimeter must pass a further selection in order to be positively tagged as photons. This selection procedure was originally developed by Mauro Verzetti in his search for the $\Upsilon(2S) \rightarrow \gamma\eta_b$ transition [17], and requires:

- The ECL cluster must not match with a charged track in the CDC
- E_9/E_{25} ratio between 0.9 and 1. This parameter is the ratio between the energy deposited in a 3x3 cluster around the most energetic crystal and a the energy deposited in the 5x5 cluster. Photons with $E < 1$ GeV are expected to generate a very compact shower that remains almost completely enclosed in the 3x3 cluster
- Shower's width less than 5.8 cm, since neutral hadrons are expected to generate showers wider than the photons' ones.

Please note that final state radiation photons are identified and removed without any quality requirement on the ECL signal.

Other not-signal photons are excluded via cuts on their energy, since it's possible to select an energy window in which a photon must lay if it comes from a real π^0 or η decay (Fig. 3.13 and Fig.3.14).

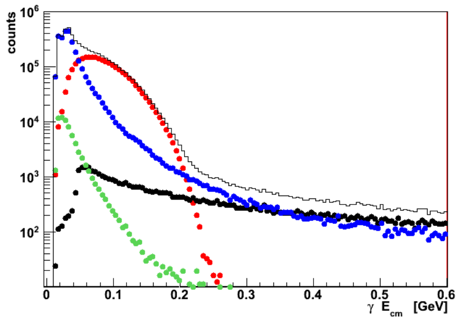

Figure 3.13: E_{cm} for γ in signal events with $\eta \rightarrow \pi^+\pi^-\pi^0$.

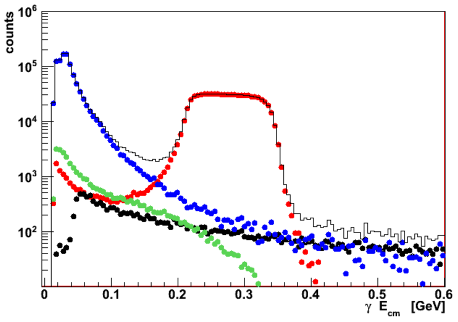

Figure 3.14: E_{cm} for γ in signal events with $\eta \rightarrow \gamma\gamma$.

For the 3-pions channel analysis we select only photons with energy in the laboratory frame greater than 57 MeV/c, in order to reject the clusters due to the beam background, and energy in the center of the mass frame less than 220 MeV/c which is the kinematic limit for this transition.
In searching $\eta \rightarrow \gamma\gamma$ the photons are required to have energy in the center of mass between 180 MeV/c and 360 MeV/c

The performances of these selection procedure are summarized in tables 3.7 and 3.8, where percentages are calculated on detected neutral entities that are not tagged as radiative photons.

Table 3.7: Radiative photons rejection efficiencies and expected counts per event of each kind of photon in $\eta \to \gamma\gamma$.

Nature	ECL cuts	ECL + Energy cut	Counts before cuts	Counts after cuts
Signal	95.58%	93.55%	1.15	1.07
FSR	57.63%	13.81%	0.04	0.005
Bremsstrahlung	66.10%	5.34%	0.09	0.004
Beam/other	85.80%	2.72%	3.23	0.09

Table 3.8: Radiative photons rejection efficiencies and expected counts per event of each kind of photon in $\eta \to \pi^-\pi^+\pi^0$.

Nature	ECL cuts	ECL + Energy cut	Counts before cuts	Counts after cuts
Signal	93.13%	77.88%	1.13	0.88
FSR	57.60%	30.02%	0.04	0.01
Bremsstrahlung	68.81%	9.72%	0.09	0.009
Beam/other	86.94%	15.52%	3.21	0.48

3.5 Best candidate selection

The quality cuts provide a list of photons and charged tracks that are compatible with the event topology and that meet some quality standards. Although the track multiplicity has been already reduced, additional cuts can be imposed to reduce the number of η candidates per event in both signal and background channels. At the end of this procedure, called best candidates selection, the maximum number of η candidates per event will be reduced to one.

3.5.1 The best π^0 candidate

Figures 3.15 and 3.16 illustrate the number of reconstructed neutral pions (i.e. the number of $\gamma\gamma$ pairs with invariant mass within 10 MeV/c^2 from the nominal π^0 mass) in $\eta \to \pi^+\pi^-\pi^0$ MC events, with no cuts applied and with all the photon cuts imposed so far applied. Clearly a further selection is required in order to select the best π^0 candidate

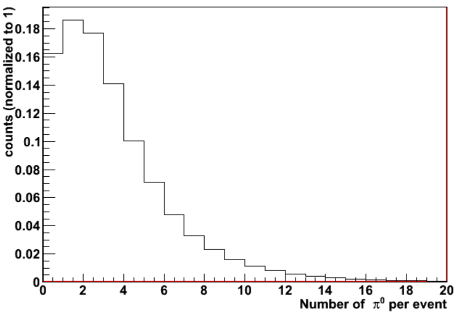

Figure 3.15: Number of reconstructed π^0's in signal MC, if all ECL clusters are used.

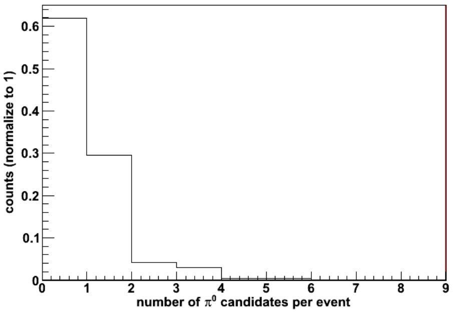

Figure 3.16: Number of π^0's reconstructed in signal MC, if only good photons are used.

The π^0 selection criterion is very simple: if an event exhibits more than one $\gamma\gamma$ pair that passed all the cuts so far, the one with invariant mass closer to the real value of $M(\pi^0) = 0.139$ GeV/c^2 is selected as π^0 coming from η decay.

3.5.2 The best $\pi^+\pi^-$ pair candidate

Further cuts are meant to suppress the fraction of $\pi^0\pi^0$ events with pair conversion into the detector of one of the four photons in the final state. The observable used to reject those events is the opening angle between the two charged pion candidates.

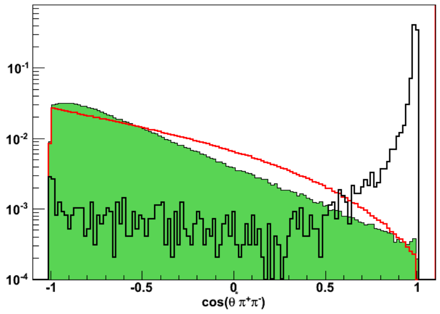

Figure 3.17: $cos(\theta^*_{\pi\pi})$ distribution.

A $\pi^+\pi^-$ candidate is required to meet the condition $cos(\theta^*_{\pi\pi}) < 0.6$ in order to be accepted as coming from the η decay.

After this selection only events with one $\pi^+\pi^-$ candidate, i.e. the events with exactly one low momentum track for each sign are selected for further analysis.
This choice is motivated by the will of keeping as high as possible the purity of the selected events: the inclusion of events with more than two low momentum tracks produces a little increase in efficiency, but also a significant loss in purity. Moreover the best $\pi^+\pi^-$ selection in events with more than one dipion candidate requires the introduction of further selection criteria (such as the $\pi^+\pi^-$ momentum or mass) that are strongly correlated with the η candidate mass.
The efficiency after this selection is 35%, dominated by acceptance loss and the cuts on the impact parameter of the low momentum tracks. Analyzing the $\eta \to 3\pi$ MC sample truth it has been possible to calculate that little fraction (1.57%) of the selected $\pi^+\pi^-$ is due, at this stage, to accidental ghost tracks.

3.5.3 The best $\eta \to \gamma\gamma$ candidate

The $\eta \to \gamma\gamma$ candidate is selected among photon pairs passing the basic photon selection described above, with the suitable energy cut. The combinatorial background from signal itself creates more than just one η candidate per event, so the first goal is to select the right $\gamma\gamma$ candidate in signal events.
Figure 3.18 shows the $\gamma\gamma$ opening angle between for both real and fake η's (reconstructed from radiative or beam photons). The real η are identified with the montecarlo truth information.

It can be clearly seen that there are no real η with opening angle between the two γ's with a cosine greater than -0.88. This feature is due to the two bodies nature of the $\Upsilon(2S)$ decay: the η is constrained to have a momentum of $p_\eta = 0.129$ GeV/c, and the γ's in the η frame have $p_\gamma = M(\eta)/2$. The effect of the combination between those two constrains is to reduces the possible values of $\theta^*(\gamma\gamma)$.
Only events with $\cos(\theta^*_{\gamma\gamma}) > -0.88$ are selected for further analysis.

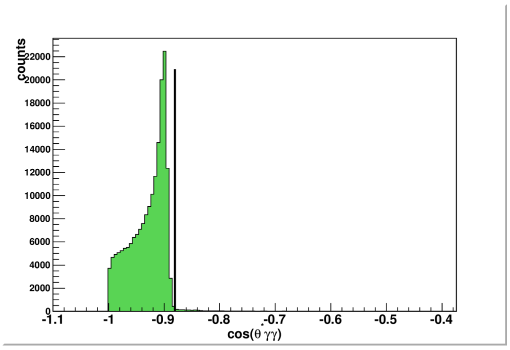

Figure 3.18: $cos(\theta^*_{\gamma\gamma})$ for real η.

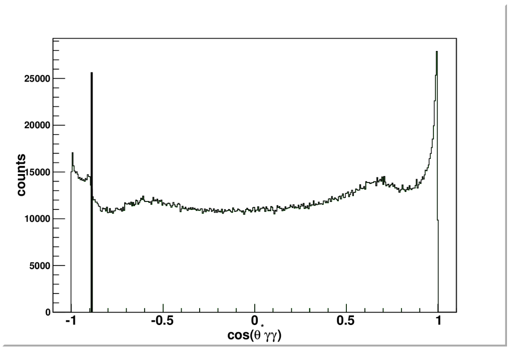

Figure 3.19: $cos(\theta^*_{\gamma\gamma})$ for fake η in signal events.

This cut, combined with the photon selection which includes the cut on the cluster energy in the CM frame, significantly reduced the number of $\eta \to \gamma\gamma$ candidates per event in the signal sample.

The contamination from fake η is, at this stage, 10.41%, while the efficiency in detecting a signal event $\eta \to \gamma\gamma$ is 50.58%, to be compared with an upper limit set by acceptance constraints of 54.33%.
Events with more than one $\eta \to \gamma\gamma$ candidate, representing the 0.5% of the selected events, are discarded.

3.6 Kinematic fit and final cuts

3.6.1 Kinematic fit

After the best candidates selection, the η candidate is searched in $\pi^+\pi^-\pi^0$ if the event shows:

- 1 di-lepton candidate
- 1 good $\pi^+\pi^-$ candidate
- 1 good π^0 candidate

While for the $\eta \to \gamma\gamma$ the requests are:

- 1 good di-lepton candidate
- no good $\pi^+\pi^-$ candidate
- 1 good $\eta \to \gamma\gamma$ candidate

The request on the number of good $\pi^+\pi^-$ candidates makes the two analyses completely orthogonal, and no cross-feed is expected.

In order to improve the resolution on the η mass distribution a kinematic fit procedure has been applied to the selected candidates.

The kinematic fit is a technique that allows to introduce constrains in an event reconstruction changing the momentum of the involved particle in order to meet them. Different kind of constrains can be imposed, usually invariant masses, vertices's position or momentum and energy conservation.

For this analysis different fitting procedures has been tested with different constrains, using the KFitter package developed by J. Tanaka and, in particular, the kmassfitter class. Since this module provides only vertices's position and invariant mass constrains, the best choice is to perform a two-step kinematic fit with mass constrain.

The first fit constrains the leptonic tracks and the final state radiation photons to have the total invariant mass of the $\Upsilon(1S)$ resonance, allowing the creation of an $\Upsilon(1S)$ candidate.

The second steps consist in a fit applied to the $\Upsilon(1S)$ candidate and the η candidate, with a mass constrain at the $\Upsilon(2S)$ mass value.

In figures 3.20 and 3.21 is shown the mass distribution of the reconstructed $\eta \to 3\pi$ and $\eta \to \gamma\gamma$ from signal Montecarlo before and after the fitting procedure:

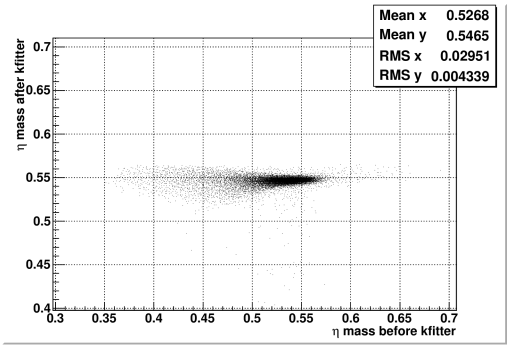

Figure 3.20: $\eta \to 2\gamma$ mass before and after the kinematic fits.

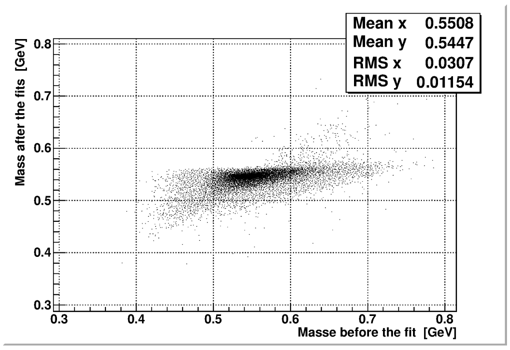

Figure 3.21: $\eta \to 3\pi$ mass before and after the kinematic fits.

The mass distribution width is improved by a factor 3 in $\eta \to 3\pi$ events and a factor 7 in $\eta \to 2\gamma$. Further cuts will be now imposed in order to reject the residual background.

3.6.2 $\eta \to \pi^+\pi^-\pi^0$ final cuts

The more conspicuous background that passes the first selection is, while detecting the $\eta \to 3\pi$ mode, due to the $\Upsilon(2S) \to \pi^+\pi^-\Upsilon(1S)$ transition. These events can be easily discarded introducing the ΔM parameter defined as the difference between the invariant mass of all the charged tracks in the event and the l^+l^- pair, which at this stage is constrained to be equal to the $\Upsilon(1S)$ mass.

$$\Delta M = M(\Upsilon(1S), \pi^+, \pi^+) - M(\Upsilon(1S))$$

Since in $\Upsilon(2S) \to \pi^+\pi^-\Upsilon(1S)$ events $M(\Upsilon(1S), \pi^+, \pi^+) = M(\Upsilon(2S))$, this observable has well defined theoretical value of $\Delta M = 0.563$ GeV/c^2 for this background. The ΔM distribution for signal and $\pi^+\pi^-$ background is shown in figure 3.22

The request of $\Delta M < 0.44$ GeV/c^2 discards the 0.89% of the signal events and the 99.92% of the $\pi^+\pi^-$ background yield.

The second and last cut exploits the χ^2 of the second kinematic fit which is directly provided by the KFitter software. The χ^2 of a kinematic fit is related to the changes imposed to the tracks; if the topology of the event has been greatly changed

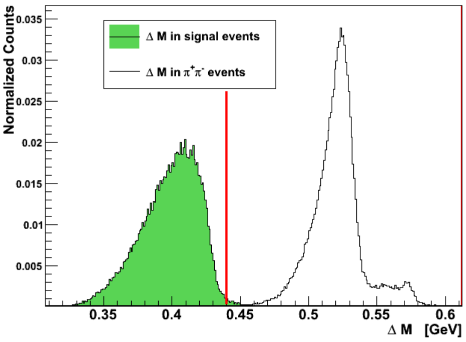

Figure 3.22: Normalized ΔM distribution for $\eta \to 3\pi$ and $\Upsilon(2S) \to \pi^+\pi^-\Upsilon(1S)$.

in order to fit the constrains, the corresponded chi^2 will have an higher value compared to an event that already fits the constrains.
The cut has been optimized separately for the two $\Upsilon(1S)$ decay mode since the continuum background is more present in the e^+e^- channel than in the $\mu^+\mu^-$ one. The two χ^2 distributions are shown in fig. 3.23 and 3.24.

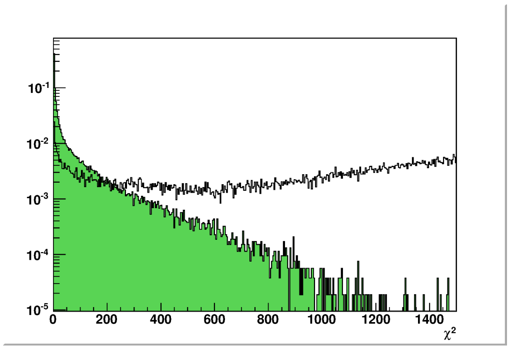

Figure 3.23: Normalized distribution of the KFitter χ^2 in e^+e^- events. The green histogram represents the signal distribution, while the black one represents the background one.

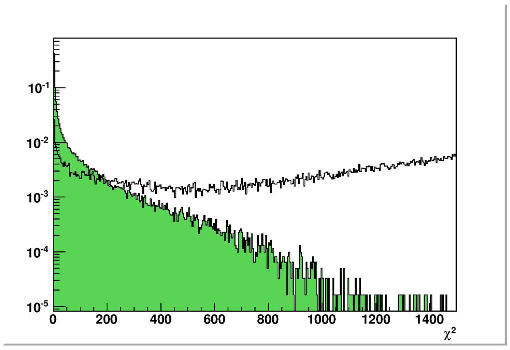

Figure 3.24: Normalized distribution of the KFitter χ^2 in $\mu^+\mu^-$ events. The green histogram represents the signal distribution, while the black one represents the background one.

Maximizing the correspondent figures of merit, an upper limit of $\chi^2 < 55$ in $\mu\mu$ events and $\chi^2 < 70$ in ee events is imposed.

Table 3.9 and 3.10 summarizes the step-by-step efficiencies in $\eta \to \pi^+\pi^-\pi^0$ selection.

Table 3.9: Final efficiencies in $\eta \to \pi^+\pi^-\pi^0$ selection,with $\Upsilon(1S) \to e^+e^-$.

Channel	Candidate selection	ΔM cut	χ^2 cut	Expected counts
Signal	9.75%	9.65%	7.59%	13.8
$\Upsilon(2S) \to \pi^0\pi^0\Upsilon(1S)$	0.0074%	0.0041%	0.0017%	6.12
$\Upsilon(2S) \to \pi^+\pi^-\Upsilon(1S)$	4.96%	0.006%	0.0005%	3.16
χ_{bj} cascade	0.004%	0.0012%	0.0006%	0.6
Continuum	0.0030%	0.0003%	0.0001%	113

Table 3.10: Final efficiencies in $\eta \to \pi^+\pi^-\pi^0$ selection,with $\Upsilon(1S) \to \mu^+\mu^-$.

Channel	Candidate selection	ΔM cut	χ^2 cut	Expected counts
Signal	11.29%	11.19%	8.55%	15.55
$\Upsilon(2S) \to \pi^0\pi^0\Upsilon(1S)$	0.006%	0.0028%	0.00073%	2.6
$\Upsilon(2S) \to \pi^+\pi^-\Upsilon(1S)$	5.61%	0.006%	0.0003%	2.1
χ_{bj} cascade	0.005%	0.0008%	0.0003%	0.29
Continuum	0.0002%	0.00007%	$< 0.00002\%$	¡22

3.6.3 $\eta \to \gamma\gamma$ final cuts

When dealing with the search for η into a γ pair and the $\Upsilon(1S)$ into e^+e^-, the primary background source is expected to be the bhabha scattering. The non radiative bhabha e^+e^- are rejected by the skim cut on the invariant mass of the dilepton, but single or double radiative events may exhibit the correct invariant mass and lepton momenta. Thus a further bhabha veto is imposed, following what has been already done by CLEO [8], rejecting events with the e^- in the forward detector region. In figure 3.25 and 3.26 is shown the cosine in the CM frame of the polar angle of the positive lepton compared to the negative one, for both electrons and muons. The data are taken from a sub-sample of the experiment 67. In the muon plot a semicircular structure due to cosmic rays passing trough the interaction region can be clearly seen.

For electrons, events with $cos(\theta^*_{e^-}) > 0.5$ are rejected; for muons no asymmetric cuts on the angular distribution has been applied. The efficiency of this cut for continuum events is 30%, while for signal events is 80%. In analogy with the $\eta \to 3\pi$

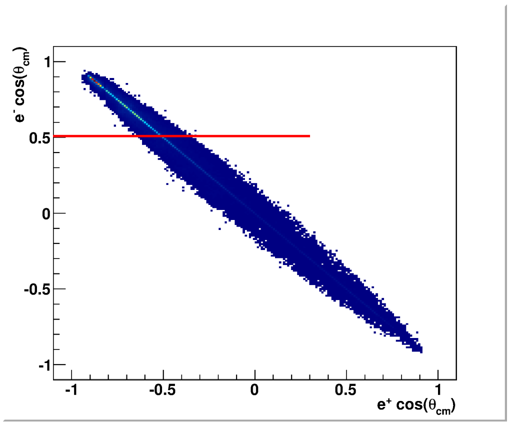

Figure 3.25: e^+ $cos(\theta^*)$ compared to e^+ $cos(\theta^*)$, in events from exp67.

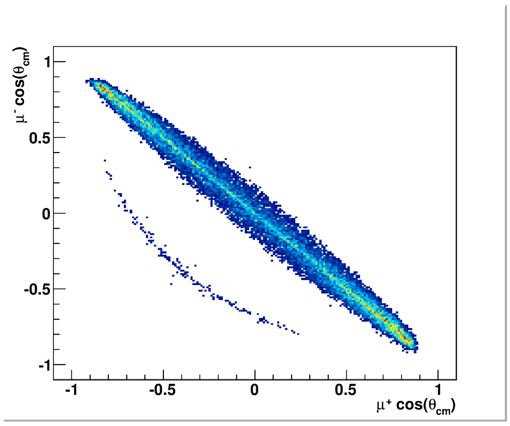

Figure 3.26: μ^+ $cos(\theta^*)$ compared to μ^+ $cos(\theta^*)$, in events from exp67.

analysis, the second cut is then applied on the kinematic fit χ^2; figures 3.27 and 3.28 show the χ^2 distributions in the two leptonic channels. The contribution coming from continuum is shown in red, while the black distribution represents the sum of all background sources.

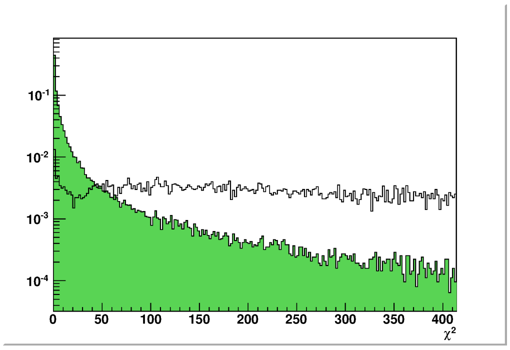

Figure 3.27: KFitter χ^2 in e^+e^- events. The green histogram represents the signal distribution, while the black one represents the background one.

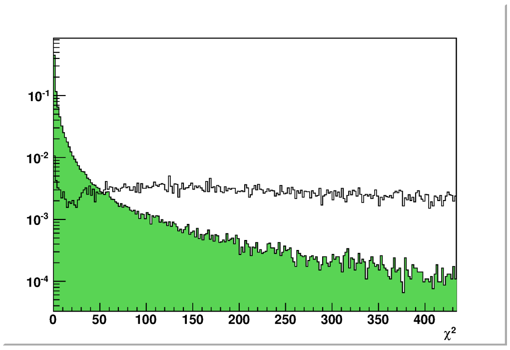

Figure 3.28: KFitter χ^2 in $\mu^+\mu^-$ events. The green histogram represents the signal distribution, while the black one represents the background one.

The maximization of the figure of merit suggests to require $\chi^2 < 9.5$ in ee and $\chi^2 < 11.5$ in $\mu\mu$ events. Since signal events must be closed the total energy in the CM frame must coincide with $\sqrt{s}$ and the total momentum must be compatible with 0. The second cut imposed is on the total momentum in the center of mass: in figure 3.29 and 3.30 is shown the momentum distribution.

The chosen cut value are $p^* < 0.07$ GeV/c in e^+e^- events and $p^* < 0.10$ GeV/c

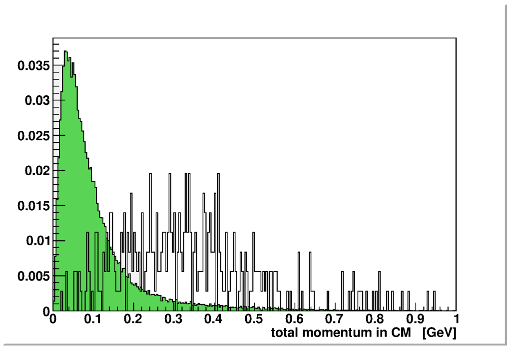

Figure 3.29: Total momentum in CM in e^+e^- events. The green histogram represents the signal distribution, while the black one represents the background one.

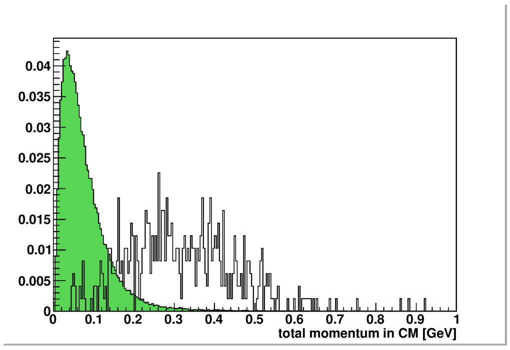

Figure 3.30: Total momentum in CM in $\mu^+\mu^-$ events. The green histogram represents the signal distribution, while the black one represents the background one.

in the $\mu^+\mu^-$ ones. Table 3.11 summarizes the step by step efficiencies in $\eta \to \gamma\gamma$ selection when the $\Upsilon(1S)$ is searched in e^+e^- mode. The $\mu^+\mu^-$ mode efficiencies are summarized in table 3.12 For both the $\Upsilon(1S)$ decay modes the main contribution is expected to come from the continuum processes.

Table 3.11: Final efficiencies in $\eta \to \gamma\gamma$ selection,with $\Upsilon(1S) \to e^+e^-$.

Channel	Candidate selection	bhabha cut	χ^2 cut	p_{tot} cut	Expected counts
Signal	41.19%	32.97%	22.98%	9.64%	30.0
$\Upsilon(2S) \to \pi^0\pi^0\Upsilon(1S)$	1.37%	1.02%	0.012%	0.0002%	0.72
$\Upsilon(2S) \to \pi^+\pi^-\Upsilon(1S)$	0.02%	0.003%	$< 0.00004\%$	$< 0.00004\%$	0.29
χ_{bj} cascade	0.046%	0.036%	0.0036%	$< 0.0001\%$	0.09
Continuum	0.068%	0.02%	0.003%	0.0001%	113

Table 3.12: Final efficiencies in $\eta \to \gamma\gamma$ selection,with $\Upsilon(1S) \to \mu^+\mu^-$.

Channel	Prel. Sel.	χ^2 cut	p_{tot} cut	Exp. counts
Signal	48.46%	35.19%	29.07%	90.69
$\Upsilon(2S) \to \pi^0\pi^0\Upsilon(1S)$	1.62%	0.020%	0.0016%	5.7
$\Upsilon(2S) \to \pi^+\pi^-\Upsilon(1S)$	0.034%	0.0058%	0.0002%	1.44
χ_{bj} cascade	0.093%	0.014%	$< 0.0001\%$	0
Continuum	0.0053%	0.001%	0.00004%	50

3.7 Fitting procedures on the montecarlo sample

The final fit is performed on the invariant mass of the η candidate; figures 3.31 and 3.32 show the invariant mass distribution for the $\eta \to \gamma\gamma$ in the two considered $\Upsilon(1S)$ decay modes, while the $\eta \to \gamma\gamma$ case is shown in fig. 3.33 and 3.34

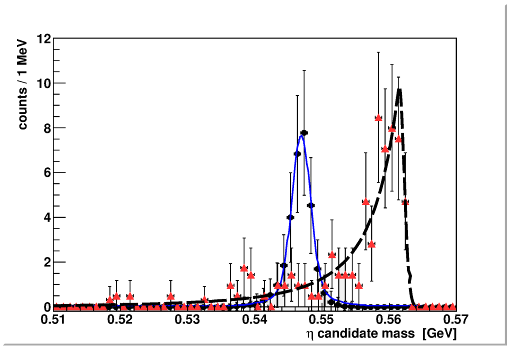

Figure 3.31: $M(\gamma\gamma)$ in events with e^+e^- pair.

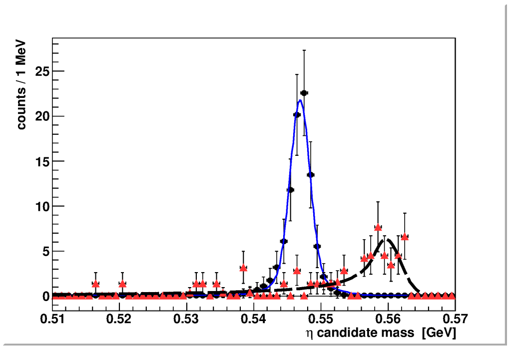

Figure 3.32: $M(\gamma\gamma)$ in events with $\mu^+\mu^-$ pair.

The signal can be fitted with a bifurcated Gaussian, and the background with a crystal ball function. Table 3.14 summarizes the fit parameters used for the $\eta \to \gamma\gamma$ channels, the fit range is $[0.51, 0.565]$ GeV/c^2.

Table 3.14 summarizes the fit parameters used for the $\eta \to 3\pi$ channels, the fit range is $[0.41, 0.565]$ GeV/c^2. The signal is fitted with a bifurcated Gaussian and the background distribution with a single Gaussian.

Table 3.13: Fit summary

Channel	Signal fit	fit χ^2/Dof
$\Upsilon(1S) \to \mu^+\mu^-$	$\mu = 0.548,\ \sigma_1 = 0.001,\ \sigma_2 = 0.004$	0.125
$\Upsilon(1S) \to e^+e^-$	$\mu = 0.547,\ \sigma_1 = 0.001,\ \sigma_2 = 0.004$	0.039
Channel	Background fit	fit χ^2/Dof
$\Upsilon(1S) \to \mu^+\mu^-$	$\mu = 0.560,\ \sigma = 0.002,\ \alpha = 0.787$	0.277
$\Upsilon(1S) \to e^+e^-$	$\mu = 0.562,\ \sigma = 0.001,\ \alpha = 0.187$	0.267

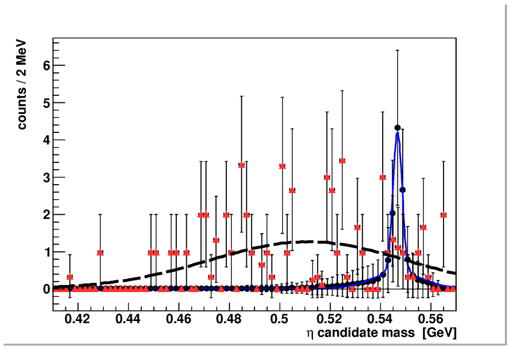

Figure 3.33: $M(\pi^+\pi^-\pi^0)$ in events with e^+e^- pair.

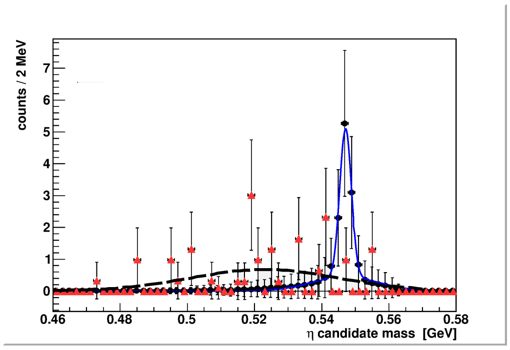

Figure 3.34: $M(\pi^+\pi^-\pi^0)$ in events with $\mu^+\mu^-$ pair.

The fit of the sum of all the four channels has been performed: figure 3.35 shows the fit on a wide range, while a close-up of the signal region is shown, with a different binning, in figure 3.36. The signal is fitted with a bifurcated Gaussian and the background with a crystal ball function.

The global efficiency on the η reconstruction is $\epsilon_\eta = (15.24 \pm 0.04)\%$ Assuming 160 millions of $\Upsilon(2S)$, the final counts in the signal box are $N_{sgn} = 116 \pm 10.77$ and $N_{bkg} = 51 \pm 7.1$, with a significance $\frac{N_{sgn}}{\sqrt{N_{bkg}}} = 16.5$

Table 3.14: Fit summary

Channel	Signal fit	fit χ^2/Dof
$\Upsilon(1S) \to \mu^+\mu^-$	$\mu = 0.547,\ \sigma_1 = 0.001,\ \sigma_2 = 0.004$	0.125
$\Upsilon(1S) \to e^+e^-$	$\mu = 0.547,\ \sigma_1 = 0.002,\ \sigma_2 = 0.01)$	0.088
Channel	Background fit	fit χ^2/Dof
$\Upsilon(1S) \to \mu^+\mu^-$	$\mu = 0.560,\ \sigma = 0.002,\ \alpha = 0.787$	0.277
$\Upsilon(1S) \to e^+e^-$	$\mu = 0.523,\ \sigma = 0.022,$	0.135

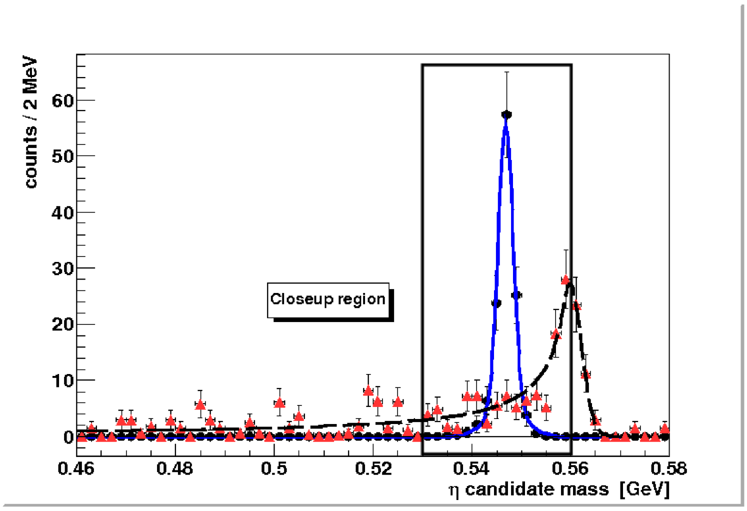

Figure 3.35: Mass distribution of the η candidates from all the four final states.

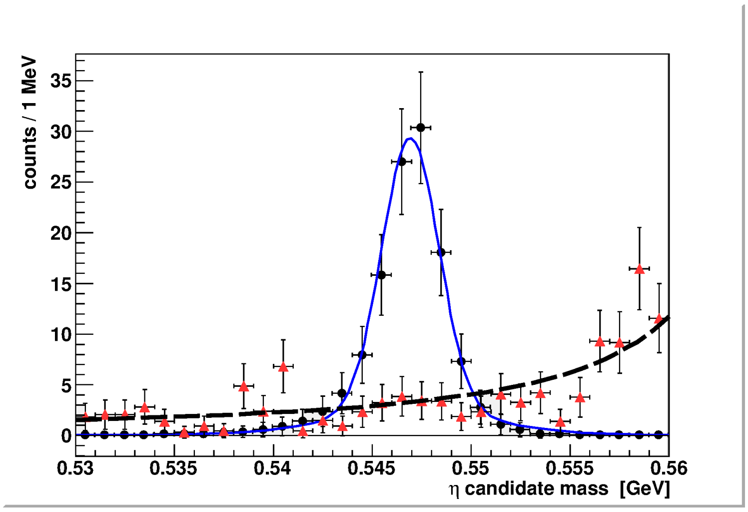

Figure 3.36: Mass distribution of the η candidates from all the four final states, signal region close-up.

Chapter 4

Data studies

In this chapter the analysis performed on the data sample will be presented. A control sample of $\Upsilon(2S) \to \pi^+\pi^-\Upsilon(1S)$ events will be defined in order to check the montecarlo normalization and quote the $R = \frac{\mathcal{B}(\Upsilon(2S)\to\eta\Upsilon(1S))}{\mathcal{B}(\Upsilon(2S)\to\pi^+\pi^-\Upsilon(1S))}$ ratio. Usign this ratio the uncertainties on the number of $\Upsilon(2S)$ candidates, together with the data recording inefficiencies, are excluded.

The sidebands in $M(\eta)$ distribution will be defined and analyzed in order to test the background simulation and normalization. A series of checks on the angular distribution of the events in the signal box is the last control performed before fit the $M(\eta)$ distribution.

4.1 $\Upsilon(2S) \to \pi^+\pi^-\Upsilon(1S)$ control sample

The $\Upsilon(2S) \to \pi^+\pi^-\Upsilon(1S)$ background is selected as normalization sample, in order to be able to quote the ratio $R = \frac{\mathcal{B}(\Upsilon(2S)\to\eta\Upsilon(1S))}{\mathcal{B}(\Upsilon(2S)\to\pi^+\pi^-\Upsilon(1S))}$.

This particular channel has been chosen since it has an high statistics, negligible background sources and a well known branching ratio $\mathcal{B} = 0.181 \pm 0.4$.

The selection criteria used are:

- No good η candidates
- Exactly 2 low momentum track
- $|\Delta z| < 3\ cm$
- $|\Delta r| < 0.5\ cm$

- $cos(\theta^*_{\pi^+\pi^-}) < 0.6$ for γ conversion suppression

The efficiency for this selection, calculated from montecarlo events, is $(42.44 \pm 0.01)\%$ in the $\mu\mu$ channel and $(36.47 \pm 0.01)\%$ in the ee one, while the background yield is negligible. The global efficiency is $\epsilon_{\pi\pi} = (39.45 \pm 0.01)\%$

Figures 4.1 and 4.2 show the agreement between the MonteCarlo simulation and the data from the whole $\Upsilon(2S)$ sample.

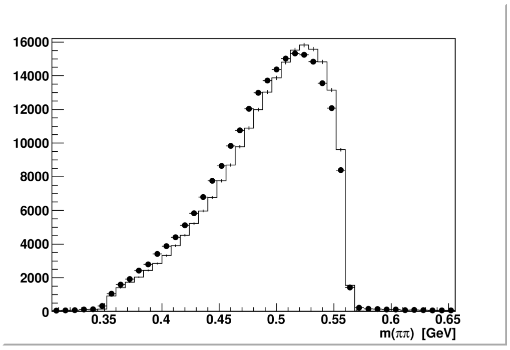

Figure 4.1: $M(\pi^+\pi^-)$ in ee events

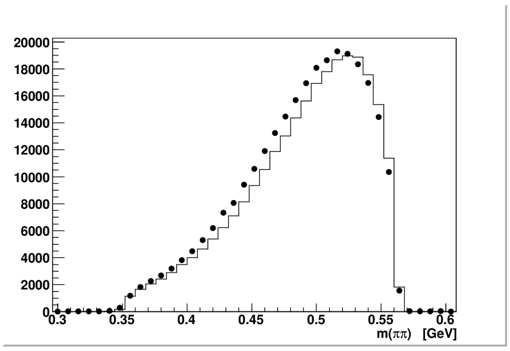

Figure 4.2: $M(\pi^+\pi^-)$ in $\mu\mu$ events

The signal distributions are compatible with the expected branching ratios and efficiencies.

4.2 Sidebands analysis

The signal band is defined by the condition 0.540 GeV/c^2 $< M(\gamma\gamma) <$ 0.552 GeV/c^2 in $\eta \to 2\gamma$ events and 0.540 GeV/c^2 $< M(\pi^+\pi^-\pi^0) <$ 0.555 GeV/c^2 in $\eta \to 3\pi$. In figures 4.3,4.4, 4.6, 4.5 the $M(\eta)$ distribution in the sidebands as can be seen in the full data sample and in Montecarlo events, for the four different possible final states, are compared.

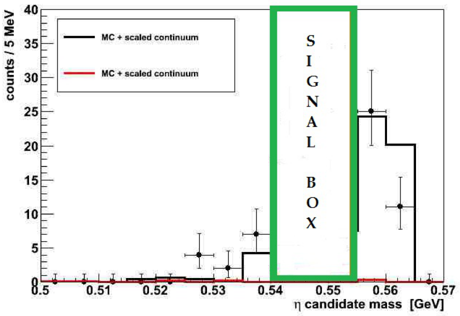

Figure 4.3: $\eta \to 2\gamma$ candidate mass in ee events

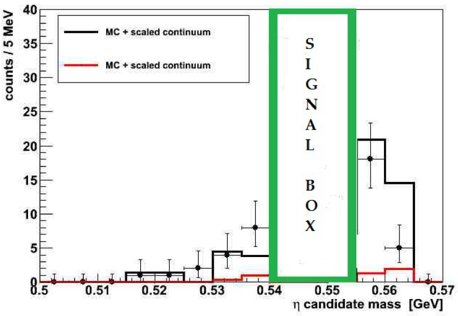

Figure 4.4: $\eta \to 2\gamma$ candidate mass in $\mu\mu$ events

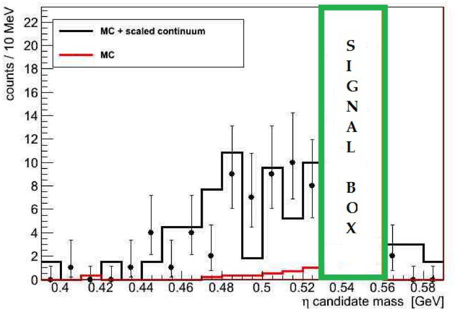

Figure 4.5: $\eta \to 3\pi$ candidate mass in ee events

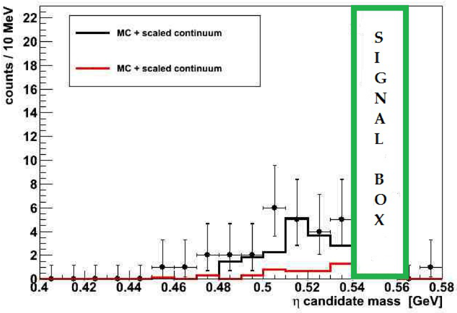

Figure 4.6: $\eta \to 3\pi$ candidate mass in $\mu\mu$ events

Table 4.1 summarizes the counts in the sidebands for Montecarlo and data, assuming 160 Millions of $\Upsilon(2S)$. Poissonian errors are understood.

Table 4.1: Counts in the sidebands, in MC and data

	DATA L. sideband	MC L. sideband	DATA R. sideband	MC R. sideband
$\eta \to 3\pi$ $\Upsilon(1S) \to e^+e^-$	70	64	10	16
$\eta \to 3\pi$ $\Upsilon(1S) \to \mu^+\mu^-$	28	21	4	2
$\eta \to 2\gamma$ $\Upsilon(1S) \to e^+e^-$	16	5	51	50
$\eta \to 2\gamma$ $\Upsilon(1S) \to \mu^+\mu^-$	18	11	31	37

All the measured yields are compatible, within the errors, with the expected ones calculated from the montecarlo and continuum sample analysis.

4.3 Signal box checks

A check on the data in the signal box has been performed in order to exclude the introduction, during the analysis procedure, of bias or correlation. Those checks are performed on observables measured in the η candidate frame. The corresponded boost obviously can not be extracted from the η momentum itself, so the two body nature of the searched decay is exploited, defining the η frame boost as the opposite of the $\Upsilon(1S)$ candidate boost; note that the cuts applied to the dileptons are completely uncorrelated to the cuts applied in the γ's or the low momentum tracks selection.

Concerning the $\eta \to \gamma\gamma$ mode, the angular distribution of the two gammas with respect to the $\Upsilon(1S)$ boost direction, measured in the η frame, has been considered. Figure 4.7 shows the distributions obtained from the e^+e^- events in real data, after all the cuts has been applied, while fig. 4.8 shows the same observable in $\mu^+\mu^-$ events.

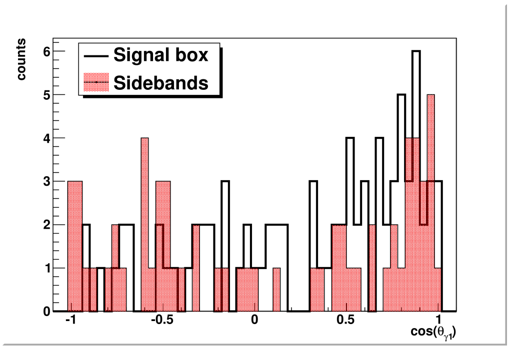

Figure 4.7: Direction of the γ's coming from the candidate η decay with respect to the DiElectron boost direction, in the η frame

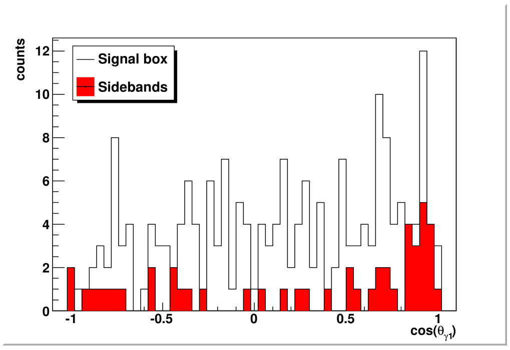

Figure 4.8: Direction of the γ's coming from the candidate η decay with respect to the DiMuon boost direction, in the η frame

The $\eta \to \pi^+\pi^-\pi^0$ events has been checked looking at the distribution, in the η frame, of the two charged pions energies. Figure 4.9 and 4.10 show those distribution in events with DiMuon and DiElectron.

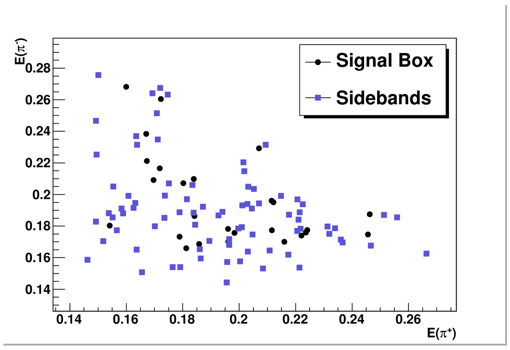

Figure 4.9: π^+ momentum compared to π^- momentum, in the η frame, in *ee* events

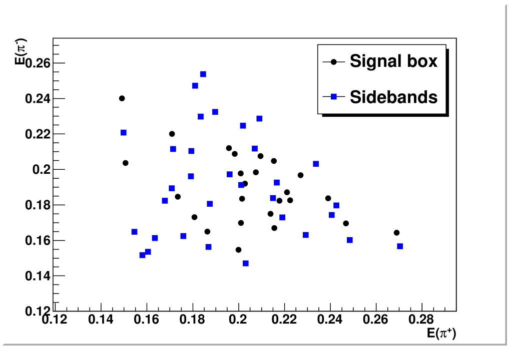

Figure 4.10: π^+ momentum compared to π^- momentum, in the η frame, in $\mu\mu$ events

No significant deviances from the expected distributions are visible.

The EVTGEN model used to simulate the $\Upsilon(2S)$ decay has been checked comparing the angular distribution of the η candidate obtained from real data in the signal box region with the Montecarlo generation.

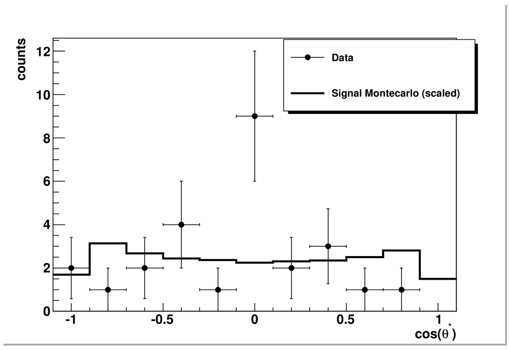

Figure 4.11: Angular distribution of the $\eta \rightarrow 3\pi$ candidates in the signal box, in *ee* events. Signal montecarlo is compared with real data

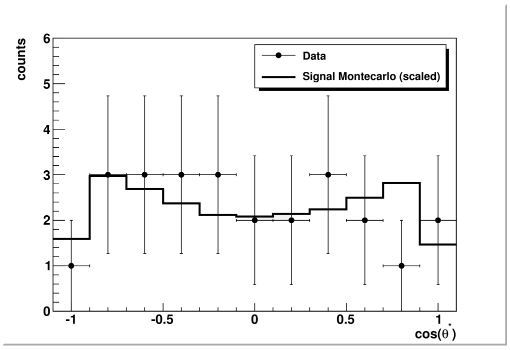

Figure 4.12: Angular distribution of the $\eta \rightarrow 3\pi$ candidates in the signal box, in $\mu\mu$ events. Signal montecarlo is compared with real data

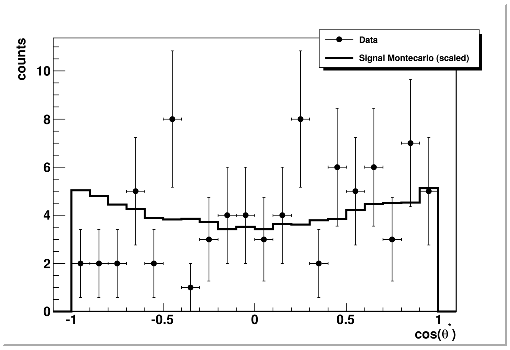

Figure 4.13: Angular distribution of the $\eta \rightarrow 2\gamma$ candidates in the signal box, in *ee* events. Signal montecarlo is compared with real data

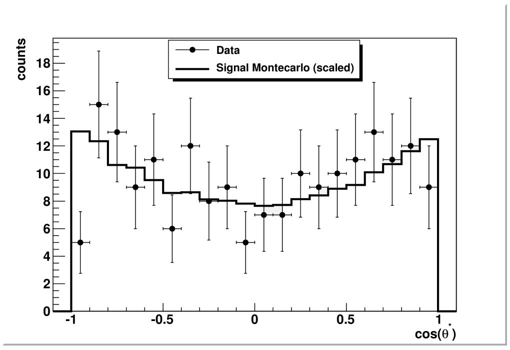

Figure 4.14: Angular distribution of the $\eta \rightarrow 2\gamma$ candidates in the signal box, in $\mu\mu$ events. Signal montecarlo is compared with real data

The angular distribution of the leptons coming from the $\Upsilon(1S)$ has been checked, since it is directly involved in the bhabha veto cut and a mismodelling can represent a major source of systematics errors in the efficiency estimation.

Figure 4.15 and 4.16 shows the distribution obtained, in the signal box region, from real data compared with the montecarlo prediction. The bhabha veto (events with $cos(\theta^*_{e^-}) > 0.5$ are discarded) is responsible for the absence of events in the $cos(\theta^*_{e^+}) < -0.5$ region in plot 4.15.

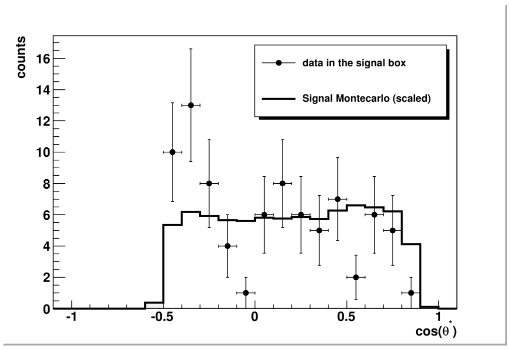

Figure 4.15: Angular distribution of the e^+ candidates in the signal box. Signal montecarlo is compared with real data

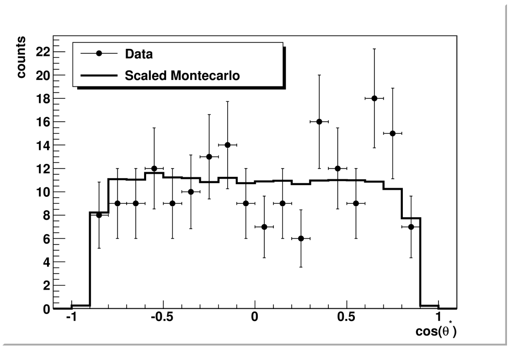

Figure 4.16: Angular distribution of the μ^+ candidates in the signal box. Signal montecarlo is compared with real data

4.4 Fit on signal and Branching ratio estimation

The Mass distribution obtained from real data can be fitted with a bifurcated Gaussian and the background with a crystal ball function.

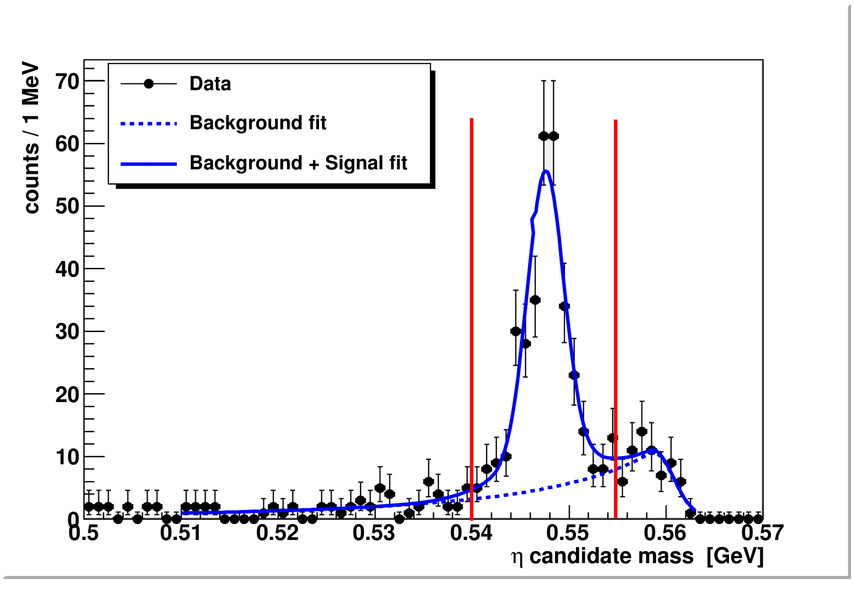

Figure 4.17: Final fit on the η invariant mass, detected in all the four final states

The parameters of the fitting functions are $\mu = 0.5475$; $\sigma_1 = 0.0018$; $\sigma_2 = 0.005$ for the bifurcated Gaussian and $\mu = 0.586$; $\sigma = 0.002$; $n = 2.44$; $\alpha = 0.174$ for the crystal ball.

The estimated yields in the signal box are $N_{sgn} = 259.39 \pm 32.56$ and $N_{bkg} =$

76.57 ± 17.88.

The $\mathcal{B}(\Upsilon(2S) \rightarrow \Upsilon(1S)\eta)$ can be calculated as

$$\mathcal{B}(\Upsilon(2S) \rightarrow \Upsilon(1S)\eta) = \frac{\mathcal{R} * \mathcal{B}(\Upsilon(2S) \rightarrow \Upsilon(1S)\pi^+\pi^-)}{\mathcal{B}(\eta \rightarrow \gamma\gamma) + \mathcal{B}(\eta \rightarrow \pi^+\pi^-\pi^0)}$$

Where $\mathcal{R} = \frac{N_{sgn}\epsilon_{\pi\pi}}{N_{\pi\pi}\epsilon_{\eta}} = 0.00133 \pm 0.00017(stat.)$ and the number of $\pi^-\pi^+$ events is $N_{\pi\pi} = 504428 \pm 710$

The estimated branching ratio for the searched transition is then

$$\mathcal{B}(\Upsilon(2S) \rightarrow \Upsilon(1S)\eta) = (3.90 \pm 0.47) \cdot 10^{-4}$$

Where the error is statistics.

4.5 Conclusions

We obtained a preliminary measurement of the branching fraction of the rare hadronic transition $\Upsilon(2S) \rightarrow \eta\Upsilon(1S)$, with the exclusive reconstruction of the final state. This result is about greater than the prediction of Ref . [10], below the value extracted from Ref. [11] and less than half the value predicted by scaling from the $\psi(2S) \rightarrow J/\psi\eta$ branching fraction [8].

A referred paper in in preparation, where the analysis on the possible sources of systematic errors will be included anc an improved result, based on the simultaneous fit of the four indipendent final states will be presented.

Chapter 5

Appendix

5.1 Radiative processes

The non resonant $e^+e^- \to l^+l^- n\gamma$ process, the radiative Bhabha scattering, is one of the main sorces of background in the study of events with leptons and photons in the final state.

The e^+e^-Bhabha scattering at $\sqrt{s} \approx 10$ GeV/c^2 is completely dominated by the electromagnetic interaction. At the tree level it can proceed in the $t-$*channel* if the final state doesn't contains electrons (such as in the $e^+e^- \to \mu^+\mu^-$ process) or in both t and $s-$*channel* if the final state consists in an e^+e^- pair.

The first order correction to these amplitudes is represented by processes with an extra photon that can be emitted both in the initial or the final state. At the second order events with two extra photons can be considered. If photons are emitted by the leptons in the initial state the process is called "Initial State Radiation" (ISR). The Final State Radiation (FSR) consists in the photon emission by the final state particles. Since the momentum must be conserved the photon emission by a lepton implies the reduction of the lepton's momentum.

5.1.1 Initial state radiation

If the emission occurs from the colliding leptons in the initial state the consequent reduction of one lepton's momentum have as consequence a reduction of the total energy in the center of mass: $\sqrt{s'} = \sqrt{s} - E_\gamma$. Therefore an high luminosity e^+e^- collider can provides, considering the ISR processes, a complete $\sqrt{s}$ spectrum up to the nominal value. The differential cross section for the production via initial state radiation of a general final state can be expressed as a modification of the non-ISR cross section σ_0 [18]:

$$\frac{\sigma_{ISR}(s,x)}{dxdcos\theta} = \frac{2\alpha}{\pi x}\frac{(1-x+x^2/2)sin^2\theta}{(sin^2\theta + m_e{}^2/E^2cos^2\theta)^2}\cdot\sigma_0(s(1-x))$$

Where $s = 4E^2$, E is the beam energy in the center of mass frame and $x = E_\gamma/E$ is the fraction of the beam energy carried by the emitted photon.
The angular distribution of the photon with respect to the lepton that emitted it is strongly peaked at low angles.
The tipical efficiency for the reconstruction of an ISR photon is $\approx 10\%$.

5.1.2 Final state radiation

If the photon emission happens in the final state one or both the leptons will have a reduced momentum without other conseguences. The final state radiation can be detected in all the final states with charged particle, in particular in the $\Upsilon(1S) \to l^+l^-$ dacay.

5.2 The Kinematic fit

The kinematic fit is a procedure that allows to determinate the best estimation for a set of given parameters, tipically the componentes of the 3-momenta of a group of particles, having imposed some constrains. The most common constrains are the four components of the total 4-momentum, the vertex position or an invariant mass value.

Consider a set of n measured values α_m with a coviariance matrix V. Let α_0 be the array containg the best estimation for the α_m parameters in presence of a set η of constrains that can be represented by k equations $f_i(\alpha_0, \eta) = 0$.
The minimization of the quantity

$$\chi^2 = (\alpha_m - \alpha_0)^T V^{-1}(\alpha_m - \alpha_0)$$

with the constrains

$$f_i(\alpha, \eta) = 0$$

gives the best estimation values α_0 of the α_m measured variables.

This problem is a vinculated optimization problem, and can be threated with the Lagrange multipliers method. It consists in minimization the non vincolated function

$$\chi^2_{NV} = (\alpha_m - \alpha_0)^T V^{-1} (\alpha_m - \alpha_0) + 2\lambda^T f(\alpha_0, \eta)$$

Where λ is an array of k unkonw parameters, one for each $f_i(\alpha_0, \eta)$, called Lagrange multiplicators. This method essentially turns the minimization of an n variables equation with k contrains in the miniziation of an equation with $n+k$ variables and no constrains.

Usually before proceed in the minimization the constrain function are linarized around an appropriate point α_p: $f(\alpha_p, \eta) + \frac{df(\alpha_p,\eta)}{d\alpha}(\alpha - \alpha_p) = 0$. The χ^2_{NV} can then be minimized obtainig the α_0 set of parameters representing the best estimation of the initial α_m parameters.

The final value of the χ^2 function itself can be used, after the fit procedure, as estimator of the fit goodness.

Bibliography

[1] J. J. Aubert *et al.* [E598 Collaboration], Phys. Rev. Lett. **33** (1974) 1404.

[2] J. E. Augustin *et al.* [SLAC-SP-017 Collaboration], Phys. Rev. Lett. **33** (1974) 1406.

[3] R. Faccini, BABAR-CONF-07/035 SLAC-PUB-13080

[4] N. Brambilla *et al.*, Eur. Phys. J. C **71**, 1534 (2011).

[5] N. Brambilla *et al.* [Quarkonium Working Group], CERN Yellow Report, CERN-2005-005

[6] E.Eichten, S. Godfrey, H. Mahlke, J. Rosner, Rev. Mod. Phys. 80:1161-1193 (2008)

[7] M. Werner, Search for new bottomonium(-like) states in $e^+e^- \to B^*\bar{B}^*\pi\pi$ at the BELLE experiment Master Thesis, Justus-Leabig Universitat Giessen (2010)

[8] Q. He *et al.* [CLEO Collaboration], Phys. Rev. Lett.**101**, 192001 (2008)

[9] T.-M. Yan, Phys. Rev. D **22**, 1652 (1980)

[10] Y. P. Kuang, Front. Phys. China **1**, 19 (2006)

[11] M. B. Voloshin, Prog. Part. Nucl. Phys. **61**, 455 (2008)

[12] B.Aubert et al., Phys. Rev. D **78**, 112002 (2008)

[13] S. Kurokawa, E. Kikutani, Nucl. Instrum. Meth. A **499**, 1 (2003). and other papers included in this volume.

[14] A. Abashian et al., Nuc. Inst. A 479 (2002) 117–232

[15] K. Nakamura *et al*(Particle Data Group), J. Phys. G**37**, 075021 (2010)

[16] D. J. Lange, Nucl. Instrum. Meth. A**462**, 152 (2001)

[17] M. Verzetti, Ricerca dello stato η_b attraverso transizioni radiative dalla risonanza $\Upsilon(2S)$ Tesi di Laurea in Fisica delle Interazioni Fondamentali, Universita' di Torino (2010)

[18] M. Benayoun, S. I. Eidelman, V. N. Ivanchenko and Z. K. Silagadze, Mod. Phys. Lett. A **14**, 2605 (1999) [arXiv:hep-ph/9910523].